Wright State University

CORE Scholar

Browse all Theses and Dissertations

Theses and Dissertations

2018

In Vitro Assessment of the Effects of Valvular Stenosis on Aorta Hemodynamics and Left Ventricular Function

Ashish Madan

Wright State University

Follow this and additional works at: https://corescholar.libraries.wright.edu/etd_all

Part of the Mechanical Engineering Commons

Repository Citation

Madan, Ashish, "In Vitro Assessment of the Effects of Valvular Stenosis on Aorta Hemodynamics and Left Ventricular Function" (2018). *Browse all Theses and Dissertations*. 1944.
https://corescholar.libraries.wright.edu/etd_all/1944

This Thesis is brought to you for free and open access by the Theses and Dissertations at CORE Scholar. It has been accepted for inclusion in Browse all Theses and Dissertations by an authorized administrator of CORE Scholar. For more information, please contact library-corescholar@wright.edu.

IN VITRO ASSESSMENT OF THE EFFECTS OF VALVULAR STENOSIS ON AORTA HEMODYNAMICS AND LEFT VENTRICULAR FUNCTION

A Thesis Submitted in Partial Fulfillment
of the Requirements for the Degree of
Master of Science in Mechanical Engineering

By

ASHISH MADAN
B.E., University of Mumbai, 2014

2018
Wright State University

WRIGHT STATE UNIVERSITY

GRADUATE SCHOOL

04/23/2018

I HEREBY RECOMMEND THAT THE THESIS PREPARED UNDER MY SUPER-VISION BY Ashish Madan ENTITLED In vitro assessment of the effects of valvular stenosis on aorta hemodynamics and left ventricular function. BE ACCEPTED IN PARTIAL FULFILLMENT OF THE REQUIREMENTS FOR THE DEGREE OF Master of Science in Mechanical Engineering.

Philippe Sucosky, Ph.D., F.A.H.A.
Thesis Director

Joseph Slater, Ph.D., P.E.
Chair, Department of MME

Committee on Final Examination

George Huang, Ph.D.

Zifeng Yang, Ph.D.

Barry Milligan, Ph.D.
Interim Dean of the Graduate School

ABSTRACT

Madan, Ashish. M.S.M.E., Department of Mechanical and Materials Engineering, Wright State University, 2018. *In vitro assessment of the effects of valvular stenosis on aorta hemodynamics and left ventricular function.*

Calcific aortic stenosis (CAS) is the most common valvular heart disease and is associated with aortopathy and ventricular dysfunction. Hemodynamic alterations due CAS could affect the aorta lining (endothelium), that is in direct contact with the blood, triggering adverse biological responses that may possibly cause aortic dilation and dissection. Also, CAS could impose excessive ventricular load leading to ventricular wall thickening, thus putting an individual at a higher risk of heart attack or stroke. These pathophysiological effects of CAS are highly dependent on the degree of calcification. However, the impact of CAS development on aorta flow and left ventricular workload remains largely unknown. Hence the objective of this study is to measure experimentally the effect of CAS on aorta hemodynamics using particle image velocimetry; and left ventricular function in terms of left ventricular work, at different stages of calcification. This study will provide insights on aorta flow abnormalities and left ventricular overload, due CAS, which can be linked to aortopathy and heart failure.

CONTENTS

FIGURES

TABLES

ACKNOWLEDGMENTS

I would like to express my gratitude towards all the people who have helped me throughout my journey at graduate school. First, I would like to thank my advisor, Dr. Philippe Sucosky, for his mentoring and guidance throughout this research. I sincerely thank all my fellow lab mates, specially Janet Liu and Jason Shar for providing their help, encouragement and advice during my research. I am also grateful towards Copey’s Butcher Shop, for supplying porcine hearts for this research. I would also like to thank my committee members, Dr. George Huang and Dr. Zifeng Yang for providing their insight on this thesis. Last but not the least, I would like to thank my parents and my sister for their love and support through the rough times.

◆

Dedicated to my mother Ashwini Madan, for her advice, her patience and her faith in me.

CHAPTER 1:

INTRODUCTION

1.1 The Human Heart

The heart is the primary muscular organ of the cardiovascular system which acts as a circulatory pump and helps in driving blood throughout the vasculature. The right side of the heart pumps blood through the lungs where it gets oxygenated. This oxygenated blood enters the left side of the heart, which supplies it to the rest of the body.

1.1.1 Anatomy

The heart is divided into four chambers (Figure 1) [1]: the two atria (right and left) and two ventricles (right and left) [2]. The atria and the ventricles are connected by the atrio-ventricular valves (mitral and tricuspid valve), while the semilunar valves (aortic and pulmonary valve) connect the ventricles to their respective attached arteries (Figure 1). The atrio-ventricular valves and the semilunar valves are responsible for maintaining unidirectional flow throughout the cardiac cycle.

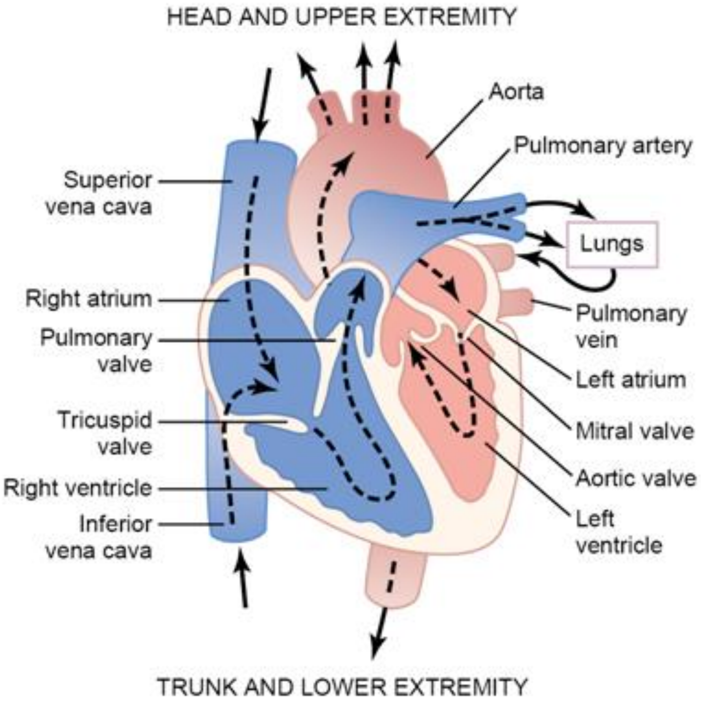

Figure 1:Schematic diagram of the heart. The arrows represent the direction of the blood flow. De-oxygenated blood from the right ventricle enters the lungs via the pulmonary artery and gets oxygenated. Oxygenated blood in the left ventricle is supplied to the e entire body via the aorta.

1.1.2 Function

The cardiac cycle is divided into two phases: systole and diastole. During the diastolic phase, (see Figure 2) the atrio-ventricular valves open and the blood flows passively from the atria into the ventricles, filling up to 80% of their end diastolic volume. The remaining 20 % is filled due to atrial contraction. The end of diastole is marked by the closing of the atrio-ventricular valves. The systolic phase begins with isovolumetric contraction of the ventricles with all the valves remaining closed. This causes the pressure in the ventricles to rise above the pressure in the arteries. A negative pressure gradient is generated across the semilunar valves causing them to open and blood to flow to the arteries. At the end of systole, all the valves close, the ventricles relax, and ventricular pressure progressively decreases back to 0 mmHg. The entire cardiac cycle lasts for 0.86 seconds for a physiological heart rate of 70 beats every minute.

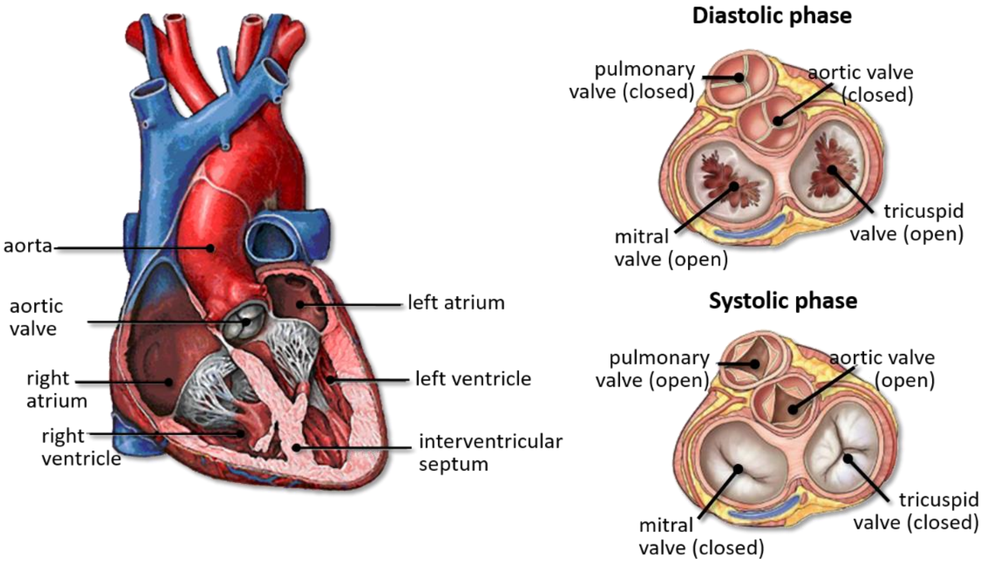

Figure 2: Schematic showing heart valve function during systole and diastole

The left ventricle of the heart is responsible for supplying oxygenated blood to the systemic circulation through the aorta. To achieve this, the left ventricle contracts, creating a peak-systolic pressure of about 120 mmHg to overcome the resistance of the systemic vasculature. Left ventricular function is assessed using two metrics: cardiac output (CO) and ejection fraction (EF). CO is the amount of blood pumped by the heart per minute. It is calculated as the product of the stroke volume and the heart rate [2]. EF is a measurement of the percentage of blood that is ejected by the ventricle of its total blood volume at each contraction. An adult human body has typically a CO of 5.0 L/min and an EF of 60 % [2]

1.2 The Left Ventricle

1.2.1 Anatomy

The left ventricle (Figure 3) [3] is one of the four chambers of the heart. It is located in the lower left portion, below the left atrium. The left ventricular chamber is connected to the atrial chamber via mitral valve, that regulates unidirectional blood flow from the atrium into the ventricle. Since it supplies blood throughout the systemic vasculature, the left ventricle has the most muscular walls of all the chambers [4]. The left ventricular wall is three times thicker that right ventricular wall. It is separated from the right ventricle by interventricular septum [5].

The left ventricle is longer and more conical in shape than the right [6]. The cross section of its cavity is oval or nearly circular in shape. The inner surfaces of the left ventricle feature irregular muscular columns called trabeculae carnea [5]. Out of the three types of trabeculae carnea, the third type musculi papillares gives rise to chordae tendinae. There are two musculi papillares, that are connected to the anterior and

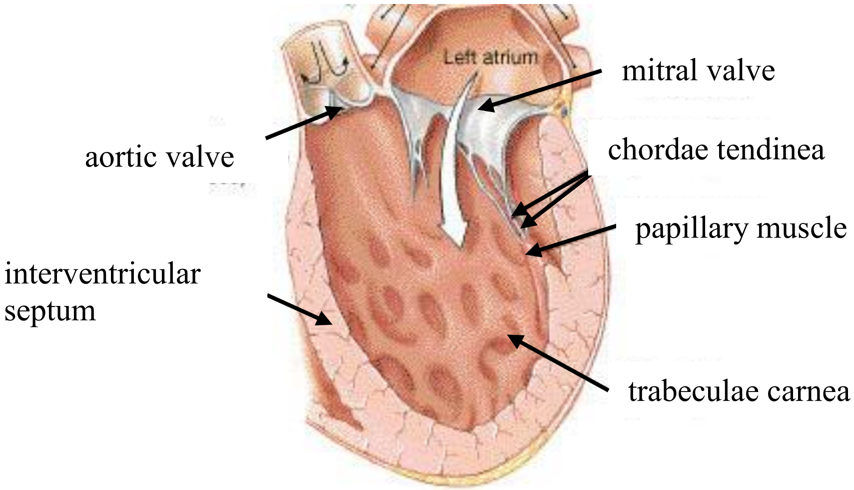

Figure 3: Left ventricular anatomy. Figure shows cross section of the left ventricle along the coronal plane.

posterior wall of the left ventricle. The chordae tendinae arising from each of the papillary muscle are further connected to both the cusps of the mitral valve (bicuspid

1.2.2 Function

The left ventricle undergoes contraction during the systolic phase and relaxation during the diastolic phase of a cardiac cycle. As the left ventricle contracts, it pushes the oxygenated blood through the aortic valve in to the AA and supplies blood to the systemic vasculature. During the diastolic phase, the left ventricular muscles are relaxed and allow for left ventricular filling with blood. The left ventricle generates a pressure of 120 mmHg at the peak systolic phase of the cardiac cycle.

1.3 The Aortic Valve

1.3.1 Structure and Function

The aortic valve (Figure 4) is located between the left ventricular outflow track and the ascending aorta (AA). The function of the aortic valve is to allow unidirectional flow between the left ventricle and the aorta. The normal aortic valve , also called tricuspid aortic valve (TAV), is composed of three leaflets (left-, right- and non-coronary leaflets), each attached to its respective sinus [7]. The sinus region consists of three cavities through which originate the left- and right-coronary arteries. The leaflets derive their respective names from these arteries [7], [8].

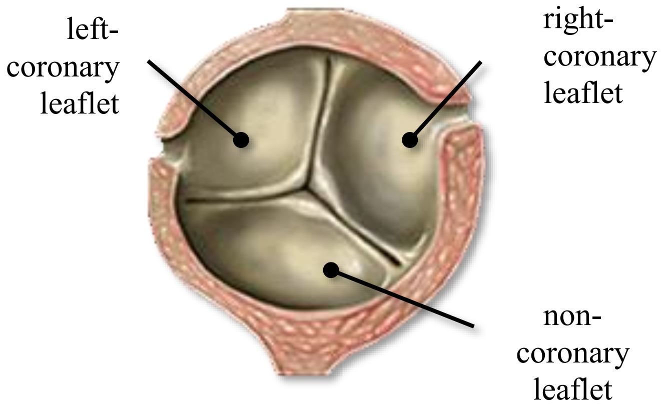

Figure 4: Schematic of the aortic valve as seen from the aorta

The leaflets consist of three different layers: the fibrosa (with circumferentially aligned collagen fibers), the spongiosa (loose, watery connective tissue containing glycosaminoglycans) and the ventricularis (with radially aligned elastin fibers intertwined with collagen fibers) [7]–[9]. The fibrosa on the aortic side of the leaflets contributes in resisting the tensile stress (Figure 5) [10] in the circumferential direction [11]. The ventricularis is the ventricular side of the valve cusp and helps in reducing the radial strains caused by the blood flow when the valve is open. [11]–[13]. The spongiosa lies between the fibrosa and the ventricularis and functions as a lubricating interface between the two other layers [10], [12].

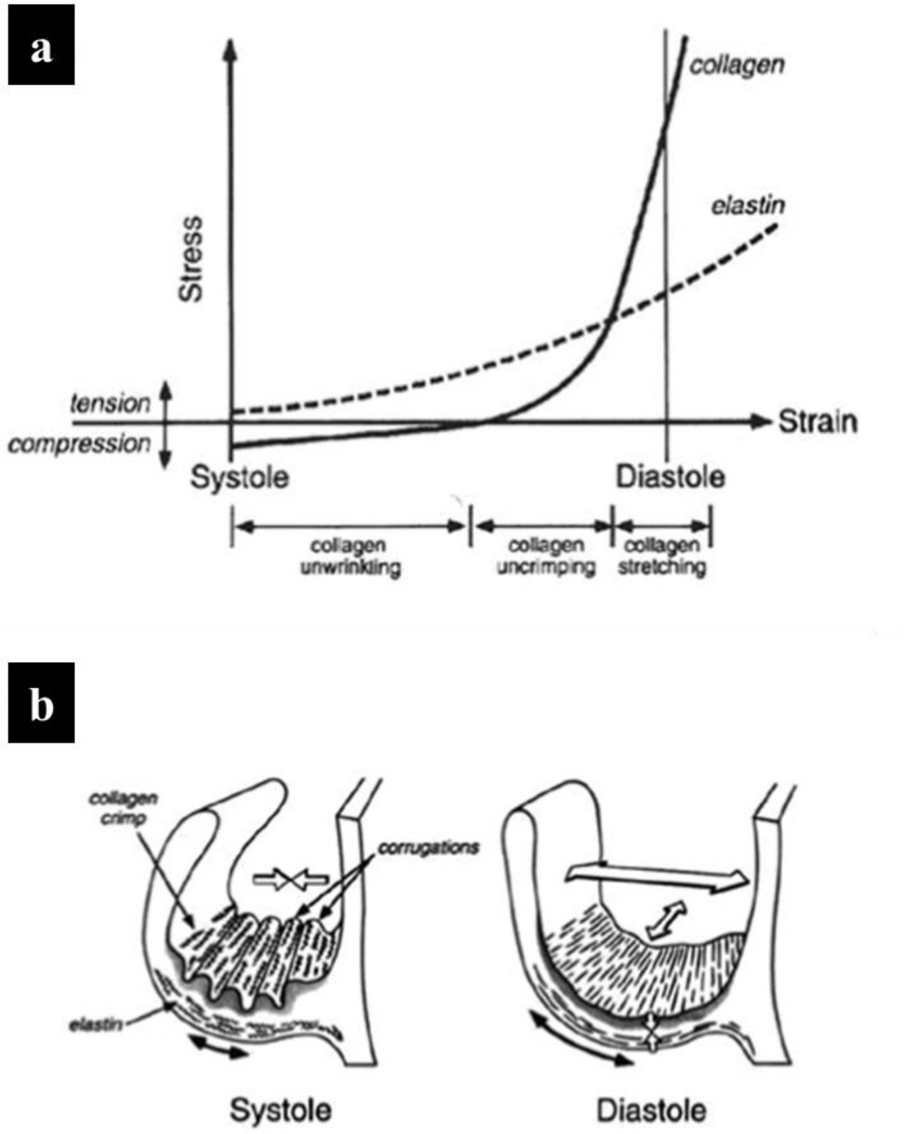

Figure 5: aortic valve leaflet and its mechanical response during systole and diastole (a) stress-strain plot for elastin and collagen fibers throughout the cardiac cycle, (b) leaflet orientation during systole and diastole

1.3.2 Hemodynamics

The dynamics of aortic valve leaflet is controlled by the transvalvular pressure gradient established between the left ventricle and the aorta. The pressure in the aorta at the end of diastole is around 80 mmHg. During the systolic phase, the left ventricle generates a blood pressure of up to 120 mmHg, which creates a negative pressure gradient across the aortic valve, causing the leaflets to open. As the ventricle relaxes, a positive pressure gradient is created across the valve, causing the leaflet to close.

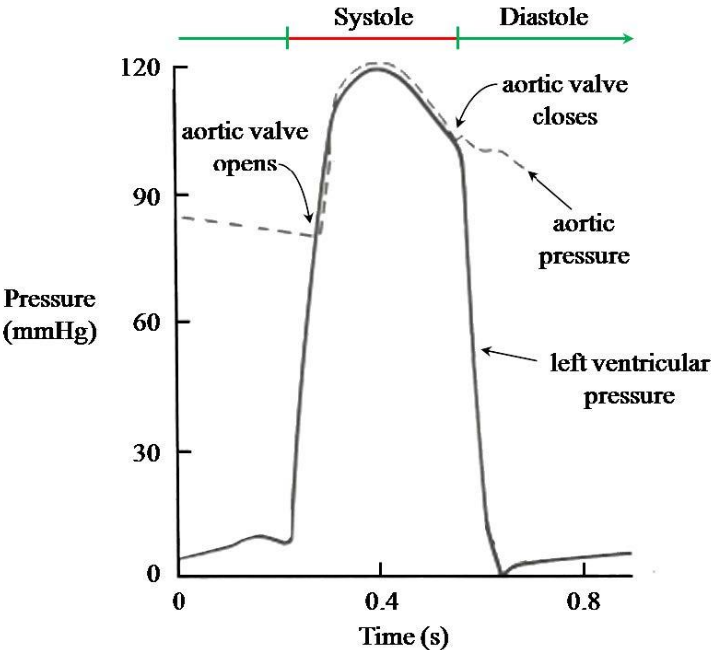

Figure 6: The left ventricular and aortic pressure waveforms. The initial systolic phase is marked with iso-volumetric ventricular contraction. A negative transvalvular pressure gradient causes the aortic valve to open, thus marking the beginning of ventricular ejection. The systolic phase ends with ventricular relaxation and closing of the aortic valve.

The aortic valve maintains a unidirectional blood flow with minimum resistance.

The blood flow behavior downstream of the aortic valve is highly dependent on the aortic valve size or the effective orifice area (EOA). The EOA is the minimum cross-sectional area of the jet emanating from the aortic valve. It is used to define the severity of valvular stenosis.

As shown in Figure 6, the ventricular contraction and relaxation facilitates the opening and closing of the aortic valve. Along with the pressure difference, the vortices formed in the sinus region behind the aortic valve leaflets also facilitate the closing of the valve cusps. Yoganathan et al. carried out an in vitro flow study through polymeric valves in a left heart simulator and demonstrated that the flow structure downstream of the aortic valve was characterized by a central orifice jet [14]. The results also highlighted the existence of a vena-contracta, defined as a contracted portion of the jet near the valve orifice. A flow separation region was observed downstream of the valve, that caused reversed flow adjacent to the aortic wall. Additionally, vortices were observed to be trapped within the sinus regions of the aorta model. The central orifice jet had a maximum peak systolic velocity of 2.8 m/s.

1.4 Calcific aortic stenosis

1.4.1 Epidemiology and pathogenesis

Calcific aortic stenosis (CAS) is the most common valvular disease in the aging population of the developed world. It is defined as a slow progressive disease with a disease continuum that starts from mild valve thickening to severe calcification of the leaflets. The initial stage of CAS, aortic sclerosis, is characterized by slow progression of fibrocalcific remodeling and thickening of the valve leaflets, without any significant obstruction to cardiac flow. Over the years, the disease progresses to severe calcification causing impaired leaflet motion and serious obstruction to blood flow [15], [16].

In CAS, the valve leaflets become thick, stiff and covered with calcific nodules on the fibrosa. The aortic valve orifice is narrowed with restricted motion of the leaflets, thus obstructing blood flow [17]. A decrease in the valve orifice diameter leads to an increased pressure gradient across the valve. This triggers the left ventricle to generate more work to fulfill the excess of energy requirement [18], leading to progressive left ventricle hypertrophy and heart failure [19]. Since the onset of CAS typically occurs in the 6th or 7th decade of the human life, it was initially described as a degenerative disorder due to leaflet wear and tear and passive calcium deposition [16], [20]. However, recent histopathological and clinical studies have demonstrated the active nature of CAS [21], by defining it as multifaceted disease condition involving lipoprotein deposition, chronic inflammation, osteoblastic transition of valve interstitial cells and active leaflet calcification [20].

CAS is the third most common cardiovascular disease after coronary artery disease and systemic arterial hypertension [15], [20], [22]. The disease can be symptomatic or asymptomatic. The patients are likely to suffer from angina, syncope or complete heart failure. Once these symptoms show up, it is difficult to predict the course of the disease, and in severe conditions, patient death is likely to occur in a couple of years [13]. CAS is a slow progressive disorder. About 1.8-1.9% of the patients suffering from aortic sclerosis (initial stage) advance towards the latter stage of CAS, which is aortic stenosis [23]. Hence, when compared with aortic sclerosis, the prevalence of aortic stenosis (AS) is much lower. While 25% of the population above 65 years of age suffers from aortic sclerosis, AS is found only in 1.7% of this population group [24]. In the general population, the prevalence of AS is 0.4%. Of all the population suffering from AS, a slight predominance of 2% was observed in men [20].

Population-based studies across the US and Europe have reported an increase in the prevalence of CAS with an increase in age [21], [25]. According to the most recent American Heart Association statistics, the prevalence of moderate and severe CAS amongst population above 75 years is 2.8% [26].

1.4.2 Clinical management

1.4.2.1 Diagnosis

Symptoms of CAS are angina, syncope and shortness of breath. Physical examination of patients with CAS have reported with a harsh systolic murmur. The onset of these symptoms along with a systolic murmur indicate the presence of hemodynamically significant aortic stenosis.

Echocardiography is an important diagnostic tool in determining the presence of CAS [27]. It helps in identifying the severity of valvular obstruction [28], [29]. Echocardiographic images of stenotic valves have shown presence of calcific lesions on the valve leaflets. Continuous wave doppler echocardiography helps evaluate the peak blood flow velocities across the aortic valve [15] . Cardiac catheterization is another diagnostic tool for the assessment of CAS. This technique evaluates the transvalvular pressure gradient by simultaneously measuring left ventricular and aortic pressure, either with single dual-lumen catheter or two separate catheters [30].

The severity of CAS can be determined by evaluating the effective orifice area (EOA) of the aortic valve, jet stream velocity and transvalvular pressure gradient. The following (Table 1) [31] classifies aortic stenosis based on guidelines provided by the American Heart Association (AHA).

Table 1: Parameters and criteria for assessment of CAS severity

	Jet Velocity (m/s)	Avg. Pressure Gradient (mmHg)	EOA (cm^2)
Mild Stenosis	<3.0	<25	>1.5
Moderate Stenosis	3.0-4.0	25-40	1.0-1.5
Severe Stenosis	>4.0	>40	<1.0

The EOA of a stenosed valve is determined by using the Gorlin equation, mathematically expressed as:

$$EOA = \frac{CO}{HR * SEP * 44.3 * \sqrt{\Delta P}},$$

where CO is the cardiac output in ml/min, HR is the heart rate in beats/min, SEP is the systolic ejection period in seconds per heart beat and ΔP is the transvalvular pressure gradient in mmHg.

1.4.2.2 Treatment

To date, the management of aortic stenosis has been limited to the surgical replacement of the aortic valve. Medical treatments have proved to be ineffective in preventing or delaying the progression of the disease [10], [15], [30], [32]. Another procedure to treat CAS is balloon valvotomy. Balloon valvotomy is a transcatheter procedure in which a balloon is positioned within the aortic valve. The balloon is then inflated causing an increase in the valve orifice area and improved leaflet mobility [30]. However, this method provides temporary relief, with patients showing signs of re-stenosis in 6-12 months and cannot be an alternative to aortic valve replacement (AVR) [10]. Thus, balloon valvotomy is used in patients who are at serious risk for surgery and waiting for an AVR [33].

Surgical intervention to replace the diseased aortic valve with a prosthesis has proved to be an efficient treatment for CAS [27], [30]. Patients with post-AVR surgeries have experienced a prolonged life with significant improvement in health [27]. A variety of prosthetic valves have been designed in an effort to mimic the native aortic valve. In an AVR surgery, the native aortic valve is first excised and then replaced with an artificial valve by suturing it to the annulus. The choice of valve (mechanical or bio-prosthetic) is highly patient-specific and depends on age, history of heart surgery, co-existing organ disease and a variety of other factors. The types of prosthetic valve are discussed below.

- Mechanical valve:

Mechanical valves have a longer lifespan as compared to bio-prosthetic valves. Mechanical valves are found to last as long as 25 years and are less frequently replaced when compared to bio-prosthetic valves [10]. There are three design types (Figure 7) [13]: ball and cage, mono-leaflet and bi-leaflet. Ball and cage valves (Figure 7a) have a ball made out of silicon, a circular sewing ring and a cage formed by three metal arches [34]. The cage was initially made from Lucite which was later changed to Stainless Steel and then Stellite 21. The sewing ring was made out of Teflon [13]. However, the ball and cage design led to increased hemolysis due to the high amount of friction that existed between the ball and the sewing ring. Thus, the ball and cage design is no longer used for AVR. However, several thousands of patients still have these valves and require a follow up [34].

The ball and cage design were replaced by the tilting disc valve (Figure 7b). The single leaflet was secured by a lateral or central metal strut [34]. The disc opened at an angle of 60^o-80^o resulting in orifices of two different sizes. This valve was made from a hemo-compatible material called pyrolytic carbon (PyC). However, it was prone to design failure as the struts could not withstand the mechanical load during the closing of the leaflet [13].

The most common mechanical valve design is the bi-leaflet mechanical valve (Figure 7c). The bi-leaflet mechanical valve consists of 2 semilunar flaps made from PyC that are hinged to a rigid valve ring [10], [35]. The leaflets open with a 75º-90º angle relative to the plane of the annulus. Once open, the two leaflets create three different orifices: a narrow slit like opening located between the two leaflets when open, and two large semicircular orifices on either side of the central opening. The bi-leaflet valve design is associated with recirculation and increased levels of shear stresses that led to hemolysis and thrombus formation [36]. As a result, patients with mechanical valves require a lifetime anticoagulation therapy.

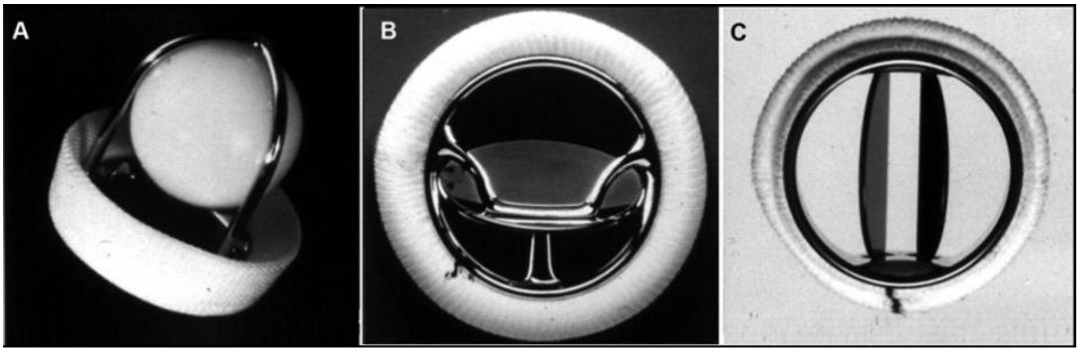

Figure 7: Different types of mechanical valves: (a) Ball and cage valve (Star-Edwards); (b) tilting disc valve (Medtronic); (c) bi-leaflet valve (St. Jude)

- Bio-prosthetic valve:

Bio-prosthetic valves (Figure 8) [13] are made of porcine tissue or bovine pericardium and are designed to mimic the native aortic valve [34]. Bio-prosthetic valve are classified as stented or stentless. A stented valve has a metal wire structure that is folded in a way to form three spikes that act an attachment site for the commissures of the valve. The entire wire frame is covered with Dacron to enable suturing of the tissue onto the stent [10]. Stentless valves are manufactured from whole porcine aortic valves or from bovine pericardium. These valves have improved valve hemodynamics as they provide a better EOA due to the absence of stent.

Figure 8: Bio-prosthetic valves: (a) Medtronic Hancock® porcine valve; (b) Carpentier-Edward PERIMOUNT Magna Ease Aortic Heart Valve and (c) Edwards Prima plus Stentless Porcine Bio-prosthesis [13]

Unlike mechanical valves, bio-prosthetic valves do not lead to hemolysis or thrombus formation and hence do not require anticoagulation therapy. However, they have a shorter lifespan as they are prone to calcification and structural failure due to mechanical stresses.

- Transcatheter aortic valve replacement

Transcatheter aortic valve replacement (TAVR) (Figure 9) [37] is a minimally invasive procedure used to replace a stenotic aortic valve [38]. About 33% of patients above 75 years of age who are suffering from CAS are turned down for AVR surgeries as surgical intervention is considered a potential risk for these patients [10]. TAVR is an option for the patients at risk from surgical AVR. In this procedure, a fully collapsible replacement valve is delivered to the aortic valve site with the help of a catheter. The catheter is inserted through the femoral artery or through the ribs from the apex of the left ventricle. Once in position, the replacement valve is expanded by pushing the native aortic valve out of the way [39].

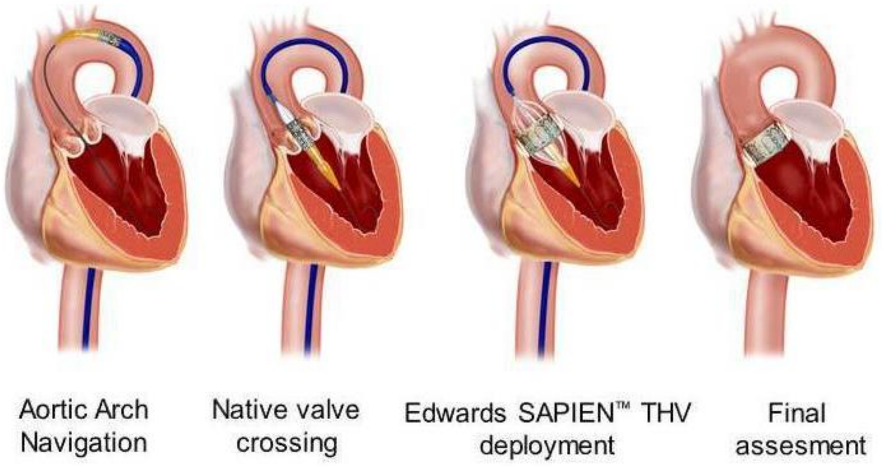

Figure 9: Implanting transcatheter aortic valve through a femoral artery. The catheter navigates through the arch of the aorta, once in place, the fully collapsible valve expands and regulates the blood flow.

1.4.3 Aortic complications

The aorta (Figure 10) [40] is the largest artery that stems from the left ventricle and extends all the way down to the abdomen [41]. It is divided into the thoracic aorta and the abdominal aorta. The thoracic aorta is further divided into four parts: the aortic root (which includes the aortic valve annulus, the aortic valve cusps and sinuses of Valsalva), the ascending aorta, the aortic arch and the descending aorta [42]. The wall of the aorta is composed of three layers: tunica intima, tunica media and tunica adventitia

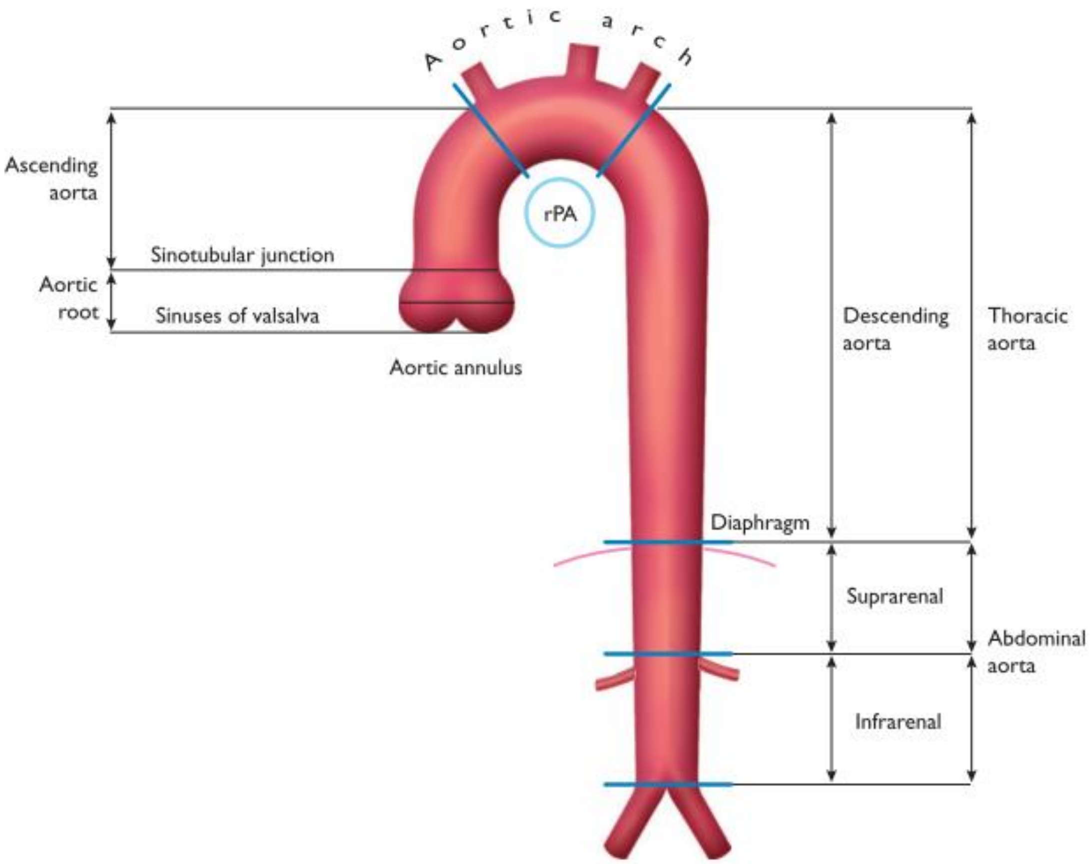

Figure 10: Sections of the thoracic and abdominal aorta.

[42]. The tunica intima is composed of endothelial cells, and this is the layer, in direct contact of the blood. The tunica media consist of elastic fibers and smooth muscle cells. The tunica adventitia is the outermost layer and mainly composed of collagen.

1.4.3.1 Aortic dilation

Aortic dilation (Figure 11) [43] is defined as an abnormal expansion of the aorta. A normal diameter for the ascending aorta (AA) ranges between 20 and 37 mm [44]. The size of the AA depends on age, sex and indexes of body size. An AA can be defined as dilated if the diameter is 1.1 times the diameter of a normal aorta [44]. The incidence of AA dilation is 5-10 patients per 100,000 patients with peak incidence between 60-70 years of age [45]. The Centers for Disease Control and Prevention rank aortic dilation as the 15th most common cause of death in patients above 65 years of age [46]. AA dilation is of two types: symmetric and asymmetric. The symmetric pattern is associated with AA of calcified TAV and is present in the mid-ascending aorta [47] . The expansion rate of dilated AA ranges between 0.75- 1.1 mm/year. Aortic dilation if not addressed can lead to dissection and rupture of the aorta.

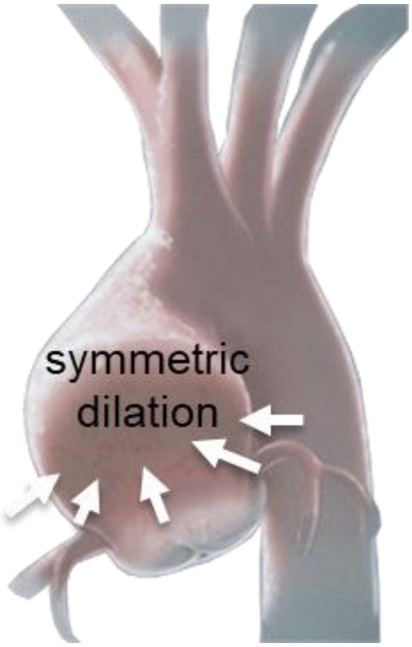

Figure 11: Symmetric pattern of aortic dilation in TAV AA.

1.4.3.2 Aortic dissection

Aortic dissection occurs when the inner layer of the aorta tears, causing the blood to flow in between the tissue layers of the aortic wall. This results in abnormal pressure over the aortic wall and may cause it to rupture. This is a potentially dangerous condition that needs immediate medical attention.

Aortic dilation has been associated with aortic dissection. Numerous studies have attempted to evaluate the risk of aortic dissection with the diameter of a dilated AA. Aortic diameter of 5.5 cm or greater [42] was considered as a risk for aortic dissection, however a clinical study involving 230 patients reports occurrences of rupture in dilated AA with diameters less than 5.5 cm [48]. Hence it is important to monitor the progression of aortic dilation. This can be done using imaging techniques such as computed tomography (CT) scan and magnetic resonance imaging (MRI) [44].

1.4.3.3 Management

Management of aortic dilation involves taking preventive measure to avoid dissection of the dilated aorta. This is achieved by surgical intervention or by using minimally invasive techniques. Surgical treatment for aortic dilation involves an open chest approach. It involves removal of the aorta tissue damaged due to dilation and replacing it with a fabric tube, called graft [49]. An alternative for surgery is a minimally invasive technique called endovascular repair for treating dilation [44]. In this technique, a catheter with an expandable stent graft is inserted through one of the groin arteries and is guided to the site of dilation with the help of X-ray images. The stent graft is allowed to expand within the aorta, while the wireframe pushes against the healthy part of the aorta sealing the graft in place [50]. The blood then flows through the graft and does not come in contact with the dilated region of the aorta.

1.4.4 Left ventricular hypertrophy

Left ventricular hypertrophy can be defined as an enlargement and thickening of the myocardial mass [21], [51]. Aortic stenosis has been associated with left ventricular hypertrophy [51]. In aortic stenosis, the reduced valve orifice, causes an obstruction to the blood flow. To overcome this obstruction the left ventricle overworks to maintain the cardiac output. This is achieved by an increase in ventricular pressure. The mechanical signals generated by the elevated ventricular pressure initiates a cascade of biological events that lead to an increase in cardiac mass [15]. Treatment for left ventricular hypertrophy due to aortic stenosis involves replacement of the stenosed valve with an artificial or tissue valve [51].

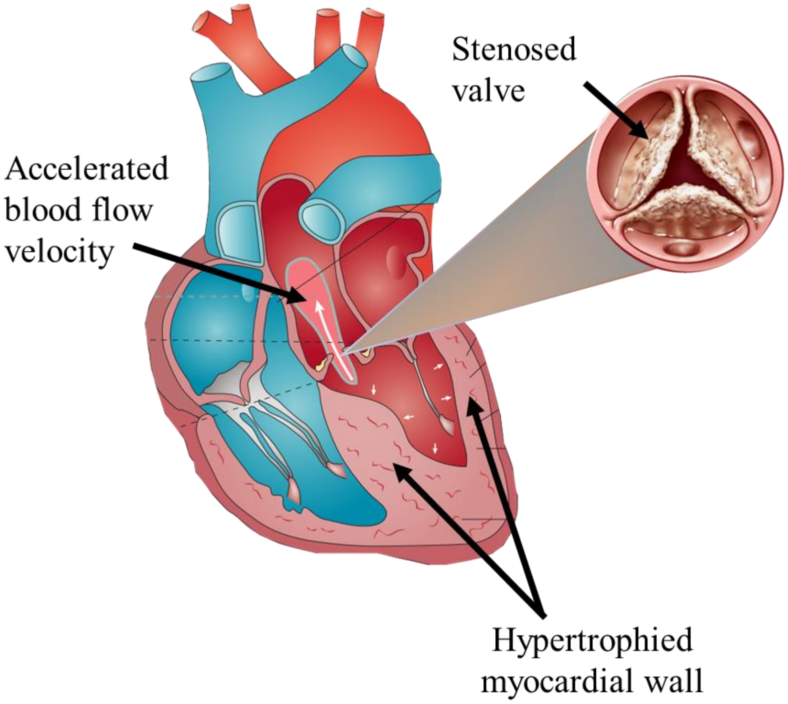

Figure 12: Figure shows sectional view of the heart with left ventricular hypertrophy

1.4.5 Evidence for a hemodynamic etiology

1.4.5.1 Aorta hemodynamics

Clinical findings have established a relation between aortic dilation and TAV associated stenosis. More than half of the patients suffering from CAS also have a dilated ascending aorta (AA) [52]. Mid-ascending aortic dilation in patients suffering from CAS is now accepted as purely hemodynamic due to TAV stenosis [53], [54]. Crawford and Roldan carried out a study that assessed the aortic root diameter of 118 patients suffering from aortic stenosis. The study concluded that aortic root dilation is common in patients with aortic stenosis. Another study assessed the rate of expansion in patients with post-stenotic dilated AA that were submitted for AVR surgery. Ninety-three patients suffering from isolated severe CAS along with dilated AA (50-60 mm) were involved in this study [52]. AVR surgery was performed and the patients had a follow-up for about 10 years. The follow-up was performed using CT scans and echocardiographic evaluations. During the 10 years, there was no significant increase in the aortic dimensions with an average expansion rate of 0.3 ± 0.2 mm/year [52]. Studies that have tracked post-stenotic aortic dilation with no valve replacement, have reported rate of expansion 10 times the rate being reported in this study [55], [56]. This study highlighted two major findings: 1) once the hemodynamic conditions were corrected by replacing the stenotic valve, no further expansion of the aorta was observed, 2) hemodynamic effect of valvular stenosis is the reason for post-stenotic aortic dilation.

Turbulent flow is believed to cause a variety of pathophysiological effects. Viscous Shear stresses due to turbulent flow are believed to cause damage to the intimal surface of the blood vessels. The existence of turbulence in the aorta was demonstrated by a clinical study involving 15 people, that analyzed the flow in the AA of humans with normal and diseased aortic valves [57]. The study highlighted that the maximum turbulence was observed in AA of patients with aortic stenosis. Histological studies of aortic wall from the post stenotic region have shown defective elastic elements and extensive areas of increased fragility [54].

An *in vitro* study by Yearwood et al analyzed the flow in a human aorta model using laser Doppler anemometer (LDA) [58]. In this study, aortic stenosis was modeled using prosthetic aortic valves attached to an acrylic aorta model in a mock circulatory system. Turbulent axial stresses determined in this study were found to increase drastically with increased stenosis. Another *in vitro* study by Yoganathan et al, found hemodynamics downstream of the stenosed aortic valve, to be dependent on the degree of stenosis [59].

A recent clinical study using 4-D flow magnetic resonance imaging (Figure 13), provided new insights on the effect of aortic stenosis on regional aortic wall shear stress (WSS) [60]. Patients with moderate and severe stenosis, with an impaired valve opening experienced increased velocities in the AA. For patients with mild aortic stenosis, a 57 % increase in the WSS was observed in the outer proximal aorta, when compared with the normal TAV patients. Further, elevation in WSS was observed in patients with moderate and severe aortic stenosis (20-178%) when compared to patients with no stenosis. The patient cohort of this study involved patients with RL-BAV (bicuspid aortic valve (BAV) with left and right coronary leaflet fusion), NL-BAV (BAV with left and non-coronary leaflet fusion), TAV, and their stenosed counterparts with degrees of stenosis, ranging from mild -severe. This study highlighted that the variability and magnitude of 3D WSS patterns is significantly higher in patients with aortic stenosis, irrespective of the valve phenotype. This study contradicts the previous findings that aortic stenosis did not elevate WSS [61], by demonstrating a significant increase in aortic 3-D WSS in the presence of aortic stenosis for both BAV and TAV groups.

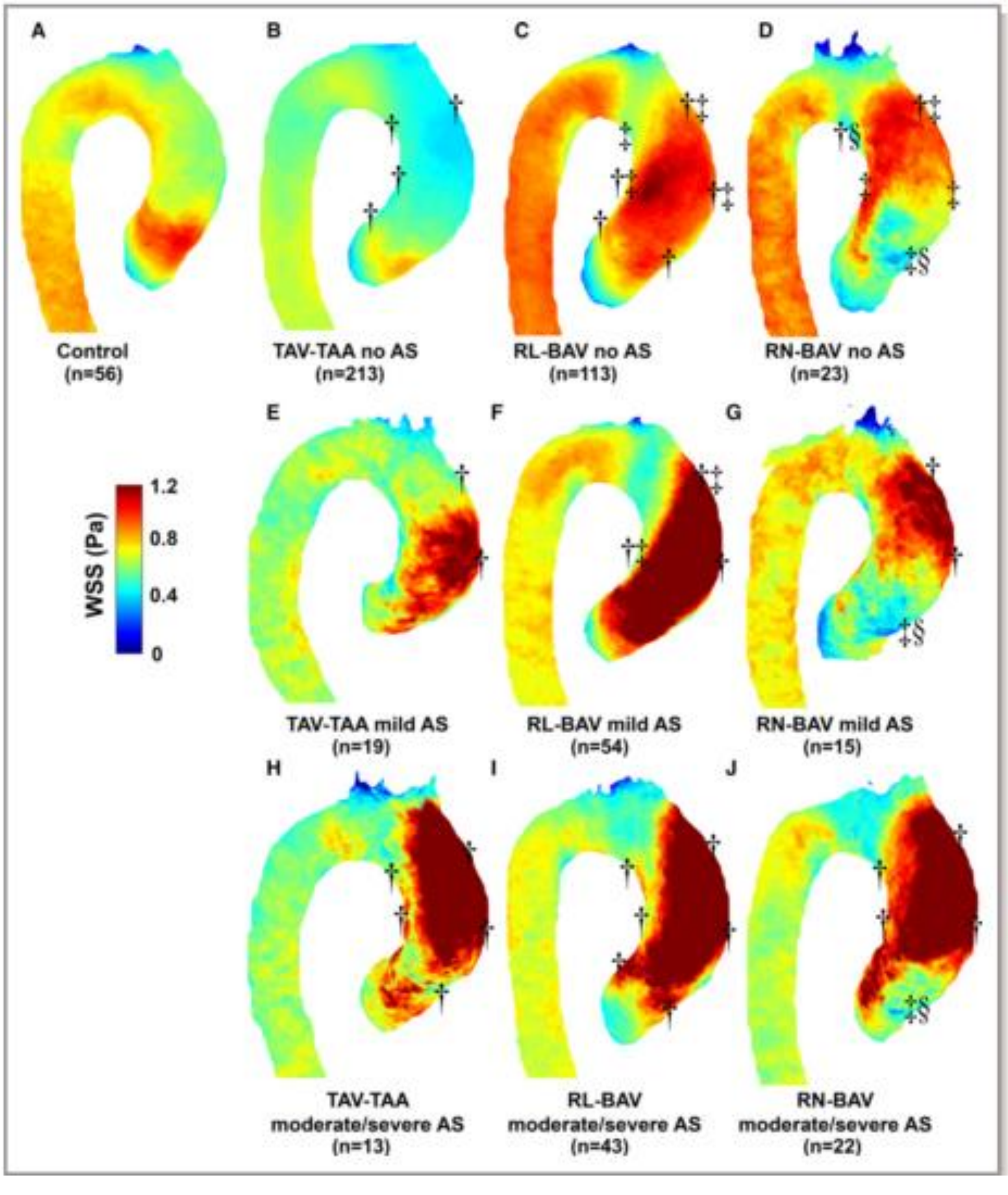

Figure 13: WSS analysis using 4-D MRI. Figure shows elevated WSS in AA with stenosed aortic valves

Elevated WSS has been previously related to pathogenic vascular remodeling that leads to aneurysm [62]. Thus, all of these clinical, imaging, in vitro and in vivo studies seem to provide compelling evidence for a possible role of hemodynamics in post-stenotic AA dilation.

1.4.5.2 Calcified valve hemodynamics

In vitro experiment, assessing the effect of varying degrees of aortic stenosis on pulsatile valvular flow, was conducted by Bluestein et al. using laser doppler anemometry (LDA) [63]. The study was conducted using polyurethane valves. The different degrees of stenosis were mimicked by gluing the leaflets together, to generate a smaller orifice. The results demonstrated a noticeable effect of aortic stenosis on the velocity profile with elevated turbulence level when compared to that of normal aortic valve.

Another flow visualization study using PIV was conducted to analyze the flow differences downstream of a normal and calcified aortic valve [64]. High orifice jet velocity and regions of increased viscous stresses accompanied by high turbulence downstream of the calcified valves were observed. With increased velocities observed at peak systole in calcified valves, high magnitudes of vorticity were observed between the sinus wall and the leaflets.

A computational study using fluid structure interaction modeling has compared the flow generated by normal and calcified aortic valve (Figure 14) [65]. The healthy model of the aortic valve generated a peak systolic velocity of 1.57 m/s, while the narrowed valve orifice in the calcified valves, led to an increase in peak orifice velocity. A significant difference was observed in the transvalvular pressure gradient, as the severely calcified valve model exhibited a 305% increase relative to the healthy model. The WSS on the leaflets was also maximum for severely calcified model.

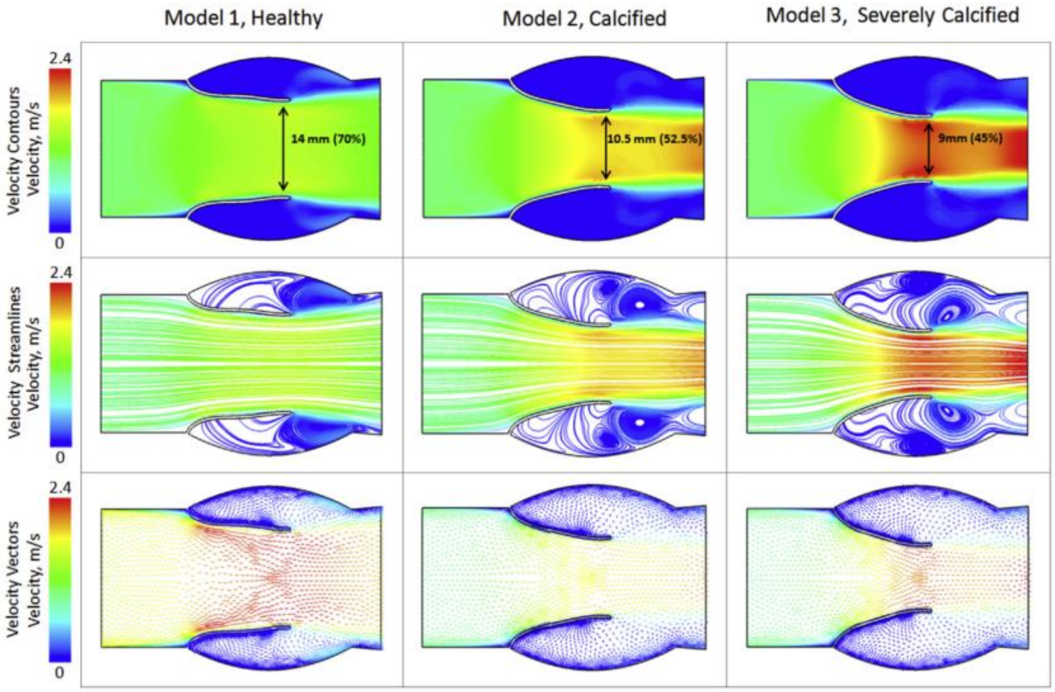

Figure 14: Figure shows the velocity contours, velocity streamlines and velocity vectors for healthy, calcified and severely calcified valve models

A clinical study evaluated the relation of left ventricular hypertrophy with systolic dysfunction and heart failure, in patients suffering from aortic stenosis [66]. It involved 137 patients with aortic stenosis undergoing pre-operative echocardiography and cardiac catherization. The findings of this study suggest that left ventricular hypertrophy promotes adverse cardiac consequences and provides a pathway towards heart failure in aortic stenosis.

1.5 Knowledge gap and research questions

1.5.1 Hemodynamic etiology of CAS

CAS has emerged as an active multifaceted disease condition whose triggers include hemodynamic, cardiovascular and mechanical factors [67]–[69]. Studies indicate that abnormal hemodynamics in the vicinity of aortic valve, experienced by the valve leaflets cause tissue inflammation, which can lead to calcification and aortic valve stenosis [70] .

The partial opening of the aortic valve due to stenosis could generate hemodynamic alterations downstream of the valve resulting in a chaotic and turbulent flow in the ascending aorta. The aorta lining in direct contact with the blood, tunica intima, is composed of endothelial cells (EC). EC are highly sensitive to hemodynamic forces and alteration in the blood flow environment have caused cell deformation, realignment and inflammation [71]. These altered biological responses due to changes in the hemodynamic environment have eventually led to aortic wall remodeling and dilation [71], [70], [72], [73]. These etiologies have been supported by studies that have demonstrated the impact of altered hemodynamics on valvular and aortic tissue [70], [74]–[77].

The aortic valve stenosis also creates an obstruction to the blood flow during the ventricular ejection. To overcome this obstruction and maintain the cardiac output, the left ventricle systolic pressure increases subjecting the ventricle to an overload. This increase in ventricular pressure to maintain the left ventricular ejection performance, initiates a surge of biological events, that ultimately lead to hypertrophy of the cardiac muscle and myocardial fibrosis [15]

1.5.2 Rationale for this study

As suggested in vivo, CAS could cause downstream flow alterations giving rise to abnormal hemodynamics. The hemodynamic theory of CAS asserts that this altered hemodynamics in the AA could cause abnormal biological responses, affecting the intimal surface of the aortic wall which can lead to aortic dilation and dissection. To validate this theory, there is a need to investigate the degree to which aorta hemodynamics is altered due to aortic valve stenosis. This study aims to assess the isolated impact of the different degrees of valvular stenosis on aorta hemodynamics.

The obstruction to the blood flow due to narrowing of the valve in CAS, affects left ventricular function. To overcome this increased resistance to blood flow, the left ventricle performs additional work to maintain a physiological cardiac output. This overload causes adverse cardiac consequences in the form of ventricular hypertrophy, increase in ventricular mass that eventually lead to heart failure. Hence it is necessary to quantify the amount of overload imposed by valvular stenosis on the left ventricle. This study investigates the effect of varying degrees of valvular stenosis on left ventricular overload.

Many studies have assessed the impact of stenosis on aorta hemodynamics. In vitro study using LDA [63] assessed the impact of stenosis on aorta flow. However, the study incorporated polyurethane valve models and a non-compliant aorta model, which could not generate native valve hemodynamics. Also, stenosis was modelled using glue lesions which questioned the accuracy of the results. To mimic the native valve hemodynamics another LDA study [78] used bio-prosthetic valves to assess the effect of valvular stenosis on aorta flow. However, the aorta model used was heavily simplified as a straight cylindrical non-compliant conduit. Lastly, PIV studies have assessed the impact of valvular calcification on the flow in the sinus region using porcine tissue valves [64], and the effect of congenitally defective valves on flow in AA [79], but the impact of calcific aortic stenosis on flow in the AA remains largely unknown.

Clinical flow visualization technique such as MRI is able to measure wall shear stress abnormalities caused by valvular stenosis in the AA [60]. However, most MRI studies have been performed in patients with pre-existing AA dilation, preventing the isolation of the effects of valvular stenosis on AA hemodynamics. Limited spatial resolution is another drawback of PC-MRI. Computational studies allow higher spatial resolution. However, these studies have significant simplification in terms of geometry and cannot assess the impact of turbulence on the flow field.

Clinical studies have associated ventricular overload due to valvular stenosis to ventricular remodeling and hypertrophy [66], [80]. However, the amount of overload imposed on a ventricle due to a stenosis has not been quantified.

Therefore, this study aims at providing insights on the isolated impact of valvular stenosis on ascending aortic flow using a non-dilated compliant silicon aorta model and left ventricular function

CHAPTER 2:

SPECIFIC AIMS

CAS is the most prevalent type of heart valve disease and is characterized by the formation of calcific nodules on the valve leaflets, resulting in the narrowing of the valve orifice. Valvular stenosis is associated with two cardiovascular complications: aortic dilation and left ventricular hypertrophy. The hemodynamic theory of valvular stenosis infers that the structural changes in the valve generate flow abnormalities downstream of the valve in the AA. These altered hemodynamics could affect the aorta lining in immediate contact with the blood surface (endothelium), triggering adverse biological responses [73] and compromising the structural integrity of the aortic wall which could possibly lead to aortic dilation and dissection [81]. Therefore, it is necessary to determine the extent to which the varying degrees of stenosis alter the hemodynamics in the ascending aorta. CAS causes reduced valve orifice. The narrowing of the aortic valve can possibly create serious blockage to the blood emanating from the left ventricle. To overcome this obstruction and maintain a physiologic cardiac output, the left ventricle has to work harder thus experiencing an additional workload. This increase in ventricular overload may lead to the thickening of the muscle wall and increase in ventricular mass. This condition is defined as left ventricular hypertrophy, which puts an individual at a higher risk for a heart attack or stroke. Hence it is important to assess the degree to which valvular stenosis creates additional workload on the left ventricle.

2.1 Hypothesis and Objective:

The hypothesis of this study is that structural changes in the aortic valve due to CAS can cause abnormal hemodynamics in the aorta and left ventricular overload. The magnitude to which aorta hemodynamics and ventricular load is altered, highly depends on the degree of valvular stenosis. Hence the objective of this study is to experimentally quantify the impact of valvular stenosis on aorta hemodynamics and left ventricular function in a degree dependent manner. This objective is addressed through three specific aims. Aim 1 describes the design of an experimental left-heart simulator and setup of a flow visualization technique called particle image velocimetry (PIV), required to investigate the hypothesis. The other two aims address the hypothesis through their respective objectives: to evaluate the impact of valvular stenosis on aorta hemodynamics (aim 2) and left ventricular function (aim 3).

2.2 **Specific Aim 1: To design an in vitro setup that mimics a physiological flow in the left side of the heart and captures the flow using PIV.**

The objective of this aim was to design a setup that allowed the assessment of the hemodynamic environment downstream of porcine aortic valve models in the AA. The flow on the left side of the heart is pulsatile due to the periodic contraction and relaxation of the left ventricle. Hence a pulsatile flow loop was needed to replicate the physiological ventricular and aortic pressures (0-120 mmHg, 80-120 mmHg) and cardiac output (5.0 L/min). The flow loop designed was validated against physiological aortic pressure and flowrate waveforms. A flow meter and pressure transducers allowed measurement of flowrate and ventricular and aortic pressures. Flow analysis was done using PIV. The PIV setup included a laser to illuminate the flow field of interest and a high-speed camera to capture images.

2.3 Specific Aim 2: To assess the effect of valvular stenosis on aorta hemodynamics.

In this aim, PIV was used to capture velocity flow fields downstream of the valve, near the sino-tubular junction as well as the AA. Velocity flow fields were captured at 43 phases of the cardiac cycle and ensemble averaging was done over 100 cardiac cycles at each phase. Along with the velocity flow field, vorticity, viscous shear stress, Reynolds shear stress and turbulent kinetic energy were evaluated from the velocity fields to compare aorta hemodynamics downstream of a normal TAV tissue model and two stenotic models mimicking moderate and severe calcification.

2.4 Specific Aim 3: To assess the effect of valvular stenosis on left ventricular function.

This aim tries to evaluate the impact of the degree of valvular stenosis on the overload imposed on the left ventricle to maintain a physiologic cardiac output. Left ventricular work was evaluated by measuring pressure-volume relationships during the ejection phase for the normal TAV and the two stenotic models.

CHAPTER 3:

MATERIALS AND METHODS

3.1 Flow loop description

A flow loop was constructed to mimic the hemodynamics of the left side of the heart. At 70 beats per min with a cardiac cycle 860 ms long, the flow conditions expected were pulsatile and periodic, with a desired flow rate at a given instant of time ranging between -5 to 20 L/min and a cardiac output (CO) of 5 L/min. The pulsatile flow loop consisted of a bath chamber, a flow meter, a compliance and resistance units and a reservoir (Figure 15). The flow was driven by a pulse generator that delivered compressed air (25 psi) to a diaphragm accumulator (AD140B25T9A1, Parker Hannifin, Cleveland, OH) mimicking the left ventricle (Figure 16). The operation of the ventricular chamber was controlled by a 2-position 3-way solenoid valve (56C-13-111CA, Mac Valves, Wixom, MI). The opening and closing of the solenoid valve was timed using a square wave signal generated by a LabVIEW (National Instruments Corp., Austin, TX) virtual instrument (VI). Unidirectional flow through the loop was achieved by installing a mechanical valve in the mitral position upstream of the ventricular chamber, and a porcine aortic valve downstream of the ventricular chamber.

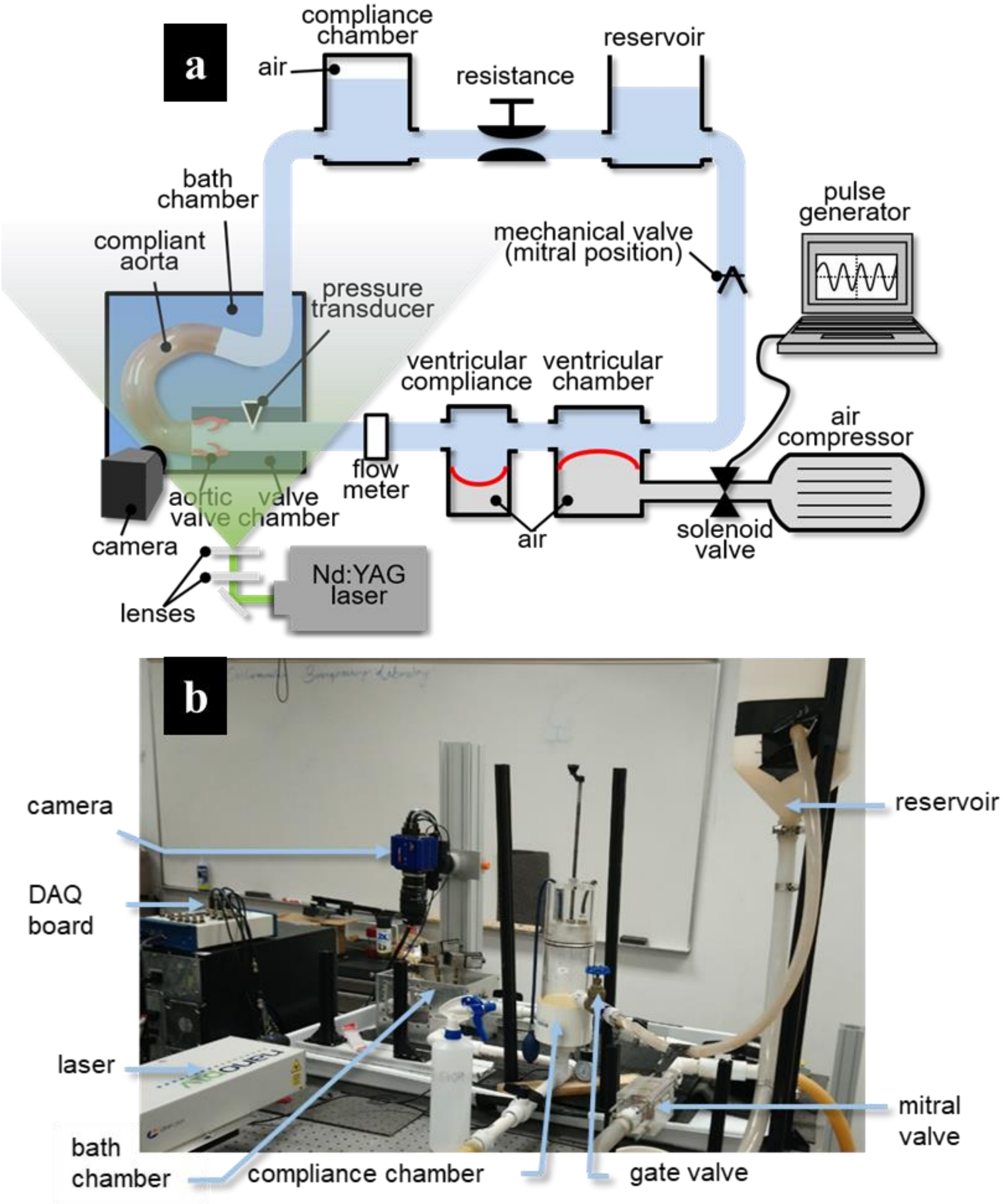

Figure 15: Pulsatile flow loop with PIV setup. (a) schematic of flow loop highlighting all its components and (b) picture of laboratory setup of the flow loop.

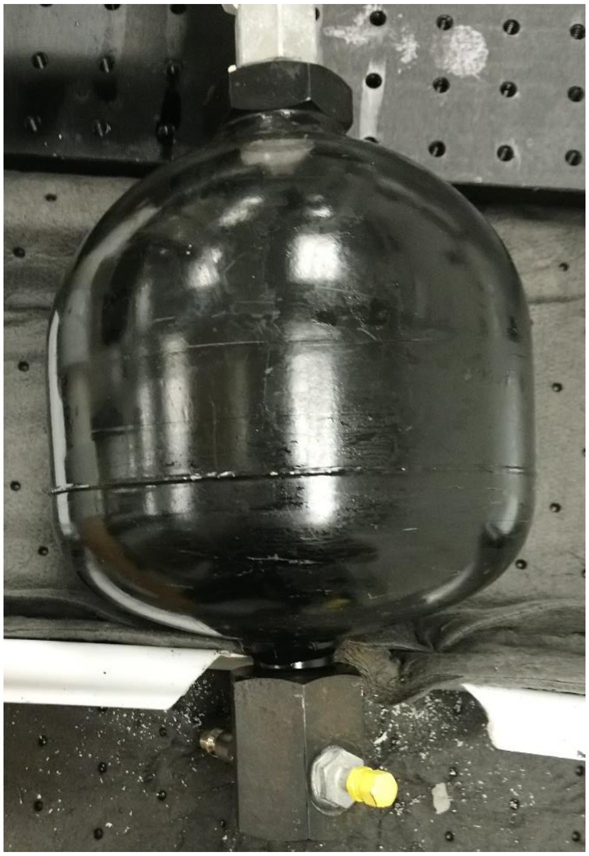

Figure 16: Diaphragm accumulator mimicking left ventricular function.

A fluid reservoir (volume: 4 L) placed between the resistance unit and the mitral valve functioned as the left atrium and supplied fluid to the ventricular chamber during diastole. Resistance and compliance units were used to achieve desired control over the pressure and flow conditions. Compliance is defined as the ability of a blood vessel to distend and increase in volume with increase in pressure. Mathematically, compliance C can be quantified as

$$C = \frac{\Delta V}{\Delta P},$$

where ΔV is the change in the arterial volume and ΔP is the change in the arterial blood pressure. The compliance chamber (Figure 17) was a cylindrical chamber consisting of a piston that controlled the ratio of air to fluid inside the chamber.

Figure 17: Compliance chamber

A gate valve (Figure 18) was used to generate vascular resistance and to control mean arterial pressure (MAP). The systemic vascular resistance (R) is the resistance to the blood flow created by the systemic vasculature. It can be defined mathematically using the Hagen-Poiseuille flow theory as

$$R = \frac{\Delta P}{Q},$$

where ΔP is the change in the time averaged pressure across an arterial segment and Q is the averaged arterial flow rate.

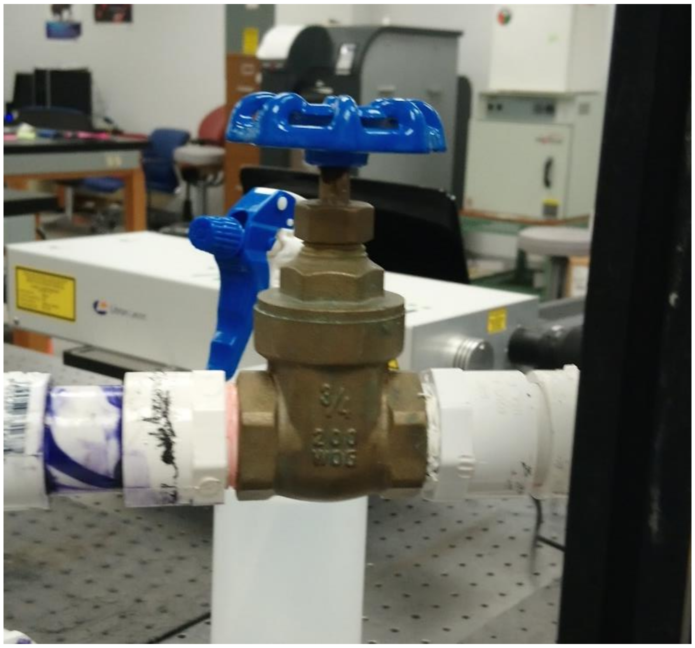

Figure 18: Gate valve used to control systemic resistance

Piping used in the pulsatile loop was constructed using PVC and silicon tubing. Two pressure transducers (P55D Validyne Engineering Corp., Northridge, CA) were used to measure the aortic and ventricular pressure. The instantaneous flow rate generated by the loop was measured by an ultrasonic flowmeter (ME-19-PXN, Transonic, Ithaca, NY) installed downstream of the ventricular chamber. The flow loop was tuned using the compliance and resistance units until a physiological cardiac output of 5.0 L/min and an approximate value of aortic pressure was achieved.

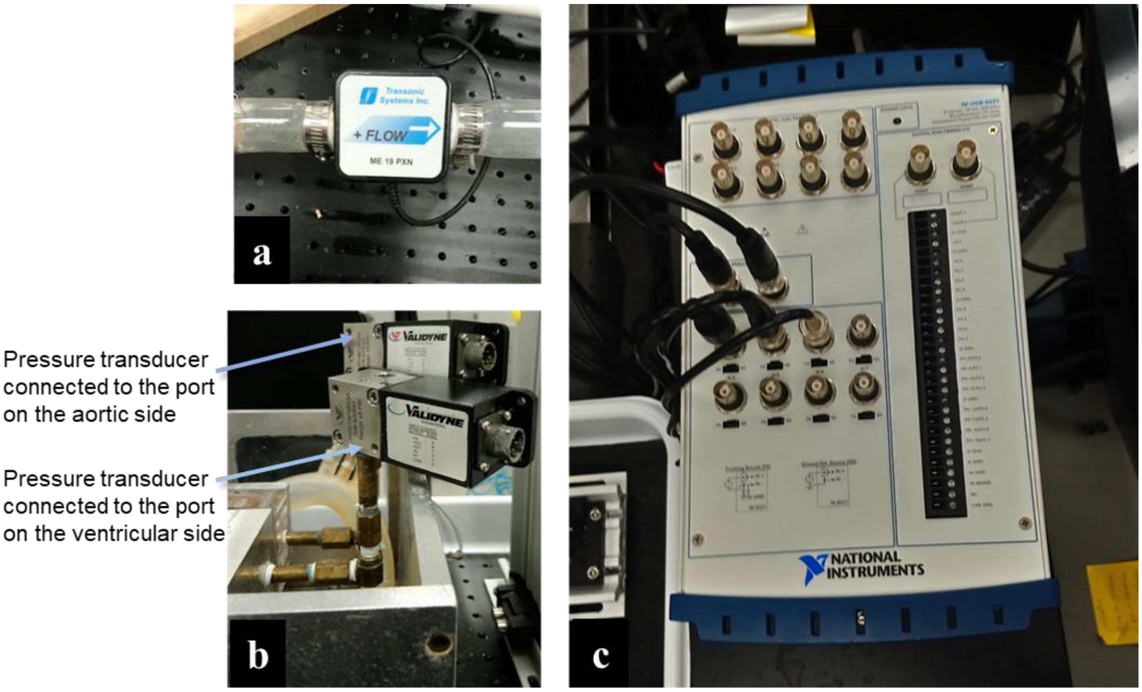

Figure 19: Figure showing components of the flow loop. (a) ultrasonic flowmeter (b) pressure transducers on the aorta and the ventricular side (c) data acquisition board

The pressure transducers (Figure 19b) and flow meter (Figure 19a) generated voltages which were analyzed by their respective modules. These modules sent analog signals to a Data Acquisition Board (DAQ) (National Instruments Corp., Austin, TX) (Figure 19c). A digital signal was generated by the DAQ board to monitor the pressure and flow rate waveforms in real time using a secondary VI. This VI also recorded the time history of instantaneous flowrate, and ventricular and aortic pressures. The flowrate and pressure values obtained were ensemble averaged.

3.2 Test section

The porcine aortic valve was placed into a valve chamber made of acrylic with flat external walls to minimize refraction of the incident laser sheet. The chamber consisted of an idealized three-lobed sinus geometry and a straight cylindrical conduit (inner diameter: 24mm, length: 20 mm) mimicking the proximal section of the ascending aorta. Pressure transducers were installed into two ports placed 24 mm upstream and 24 mm downstream of the aortic valve sinus, measuring the aortic and ventricular pressure respectively. The valve chamber was connected to a compliant silicone aorta model. The aorta geometry (Medisim Corp. Inc., Alton, ON) was 3D printed using a silicone material. The aorta model and the valve chamber were submerged in a rectangular bath chamber (Figure 20), filled with a solution of water and glycerol (BDH1172 VWR ANALYTICA) (water: 60% and glycerol: 40%, by volume). The properties of this solution (density: 1060 kg/m^3, dynamic viscosity: 3.8 cp) approximated the properties of blood (density: 1060 kg/m^3, dynamic viscosity: 3.5 cp) and provided partial index matching (refractive index: 1.39) with silicone (refractive index: 1.41) and acrylic valve chamber (refractive index: 1.49).

The bath chamber featured an inlet port that connected to the inlet of the rectangular conduit and an outlet port that connected to the outlet of the aorta model. The rectangular conduit connected to the inlet of the valve chamber

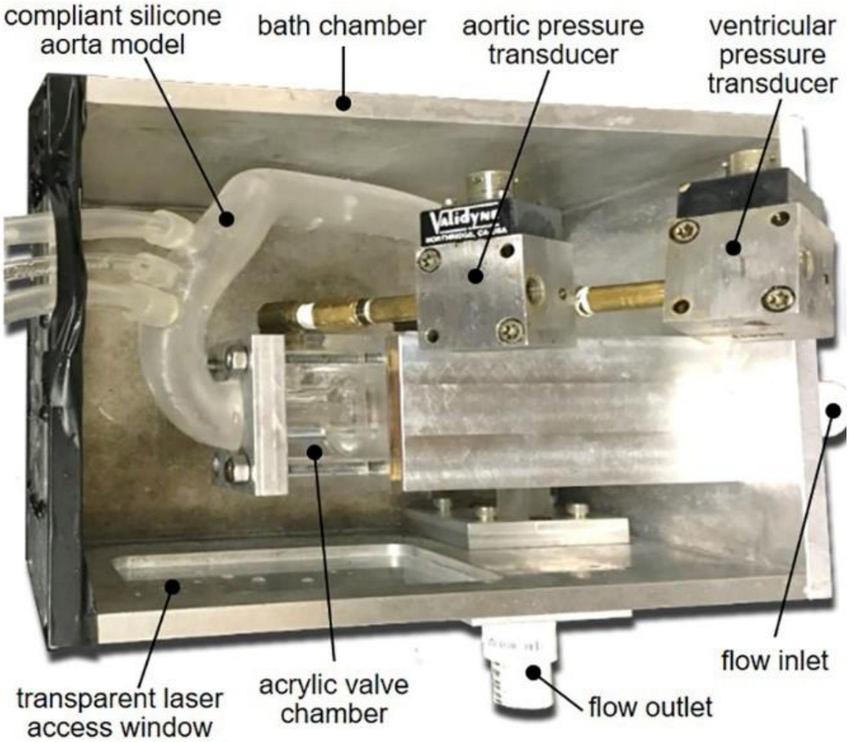

Figure 20: Figure of the bath chamber showing the valve chamber connected to the compliant silicone aorta, and the two pressure transducers used to measure aortic and ventricular pressures.

3.3 Valve models

Three aortic valve models were constructed for this study: a normal TAV model (nTAV) and two stenotic models mimicking moderate (mTAV) and severe (sTAV) calcification. Porcine hearts were obtained from a local slaughterhouse (Copey’s Butcher House, Medway, OH) and were transported to the laboratory in ice-cold phosphate buffered saline (PBS). Upon arrival, the valves were excised from the hearts and were kept moistened via frequent application of PBS solution. Excision consisted of separating the valve from the base of the aorta. The following step consisted of removing the excess ventricular muscle around the sinus region and suturing the valve on the circular supporting base plate of the valve mount. To maximize optical access to the valve, the sinus wall was surgically removed without damaging the valve leaflets. All experiments were conducted within 48 hours of procuring the organ.

3.3.1 Normal TAV model

The normal TAV (nTAV) model (Figure 21) was constructed by removing the excess muscle around the valve annulus. The valve was fixed on the circular shaped valve mount using surgical sutures. The valve posts assisted in keeping the commissures in place and maintain the leaflet orientation.

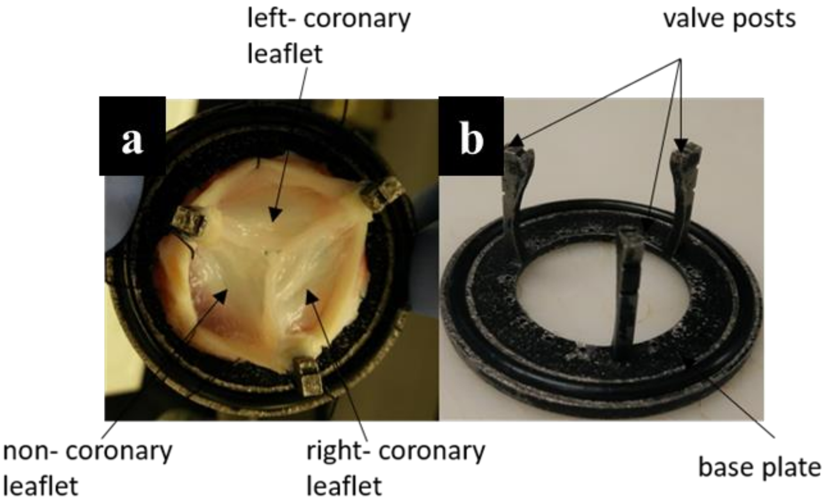

Figure 21: Figure shows (a) a normal TAV (nTAV) sutured on the valve mount, (b) circular metallic valve mount.

3.3.2 Calcified TAV models

Calcified valve models (Figure 22) were fabricated to replicate moderate and severe calcification via partial commissural fusion. Once the valve was placed onto its circular mount, partial commissural fusion was achieved by suturing together the adjacent edges of the leaflets. The two degrees of stenosis were obtained by suturing the leaflets over a length of 4 mm (mTAV) and 8 mm (sTAV) away from the valve posts towards the leaflet tip, respectively.

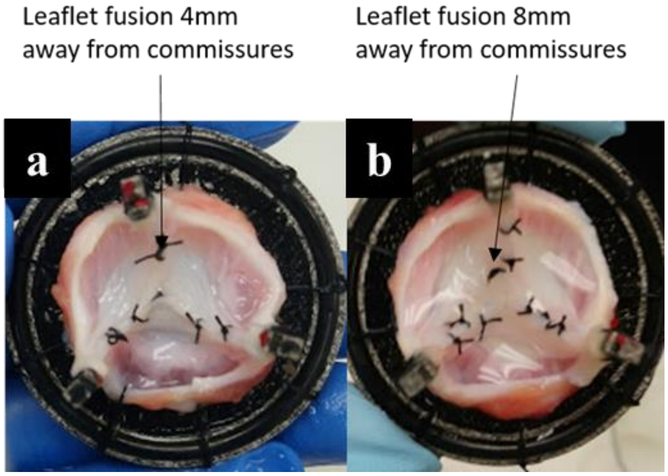

Figure 22: Pictures of stenosed valve models. (a) mTAV and (b) sTAV models. Picture also highlights the variation in the placement of sutures over the leaflets to mimic different degrees of stenosis.

3.4 Particle Image Velocimetry

Particle Image Velocimetry (PIV) is a flow visualization technique that measures instantaneous velocity flow fields by recording images of suspended seed particles in the flow at successive instants of time (t) and ($t + \Delta t$). The layout of a PIV setup is shown in Figure 23. The first step in PIV is to seed the working fluid with tracer particles. A pulsed light source and its necessary optics used to generate a thin sheet of laser illuminates a cross-section of the flow while a camera captures image pairs at a given frequency. Software and electronic equipment helps to synchronize the pulsing of the laser with the frame rate of the camera.

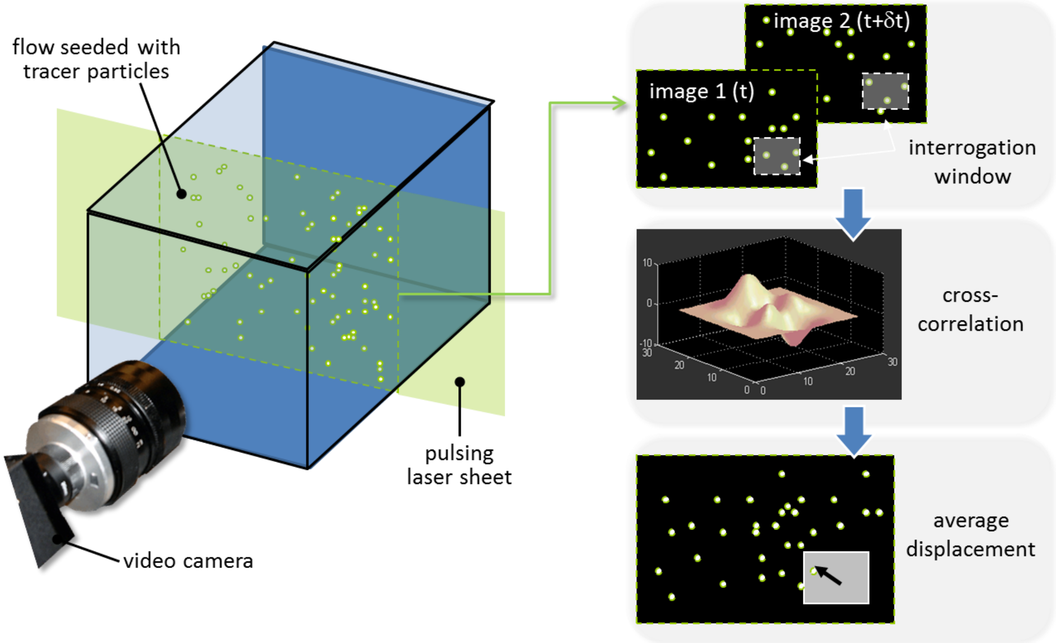

Figure 23: Schematic showing setup and functioning of PIV.

In PIV, the velocity of the flow field is extracted from the motion of the tracer particles. The velocity is calculated indirectly, by measuring the displacement of the tracer particles in a time interval Δt between the two successive image pairs. However, the displacement of the particles is not calculated on a single particle level, the flow field of interest is divided into smaller sections called interrogation regions or windows. The interrogation window is the region where cross-correlation is performed.

The images captured by the camera in PIV are greyscale digital images. The gray level for the camera sensor is defined using bits, and the number of levels per pixel are evaluated as 2^{bit}. In general, particle images are grayscales with a wide range of intensities (256 for an 8 bit camera, 65536 for a 16 bit camera). These intensity values of each pixel, from the first and the second image of the image pair, are used to perform cross-correlation.

The flow velocity is evaluated at equidistant grid points in PIV. The interrogation window is centered on these grid points. Once the interrogation region is defined, the displacement function of the tracer particles outlining the motion of the particles from the first image (time t) to the second image (time $t + \Delta t$) is calculated by a cross-correlation technique. The correlation value is evaluated by the number of overlapping particle in the spatially shifted image [82]. The location of the highest correlation value in the correlation plane, is interpreted as the mean displacement of the particles in that region. Direct cross-correlation is expensive in terms of required computing power. Hence, the correlation is done using efficient fast Fourier transform (FFT) algorithm.

The average velocity is then evaluated by dividing the mean displacement of the particles by the time interval Δt between the two consecutive images. Once the velocity is evaluated, the center of the interrogation window is shifted to the next grid point, thus a two-dimensional velocity field is obtained.

The size of the interrogation window plays an important role in the PIV measurements. The reliability of the cross-correlation method is highly dependent on the number of overlapping particles that exist between the two interrogation windows, centered on the same grid point of the image frames taken Δt apart. A small number of overlapping particles questions the accuracy of the mean displacement evaluated. Hence to maximize the accuracy of the measurements, an overlap is introduced between two consecutive interrogation windows. Overlap determines the grid of the velocity vector or the distance between the two adjacent velocity vectors. Overlap improves spatial resolution. PIV studies conducted have shown that a 50% or 75% overlap is common [82] [83].

Advanced evaluation methods have been incorporated to improve the accuracy and resolution of the PIV results. PIV images can now be evaluated using a multi-pass algorithm. In this method, an initial estimate of particle displacement is provided by a large size of interrogation window. This estimate is used to displace or deform the interrogation region used in the next pass. This technique allows to deviate from the quarter rule (all displacements should lie within 1/4th of the interrogation window size), thus providing the use of a smaller interrogation window size and improved spatial resolution.

3.4.1 Tracer particle deposition speed

The assumption that particles passively follow the flow is incorrect, since the particles are subjected to unsteady flow effects and can possibly have a velocity relative to the flow. Hence it is necessary to evaluate the deposition velocity of the tracer particles used in the PIV setup. This can be done using the Stoke’s settling velocity of the particles given by:

$$v_{\max} = \frac{2}{9}\, r_p^2 \left(\frac{\rho_p - \rho_f}{\mu}\right) g,$$

where r_p is the particle radius, ρ_p is the particle density, ρ_f is the fluid density, μ is the dynamic viscosity of the fluid and g is the acceleration due to gravity. The particles used in this study had a diameter of 11.7 μm and a density of 1100 kg/m^3. The density of the working fluid was 1060 kg/m^3 and viscosity of 3.8×10^{-3} kg/m.s. The acceleration due to gravity was taken as 9.81 m/s^2. Thus, the tracer particle deposition speed evaluated was 0.785 μm/s

3.4.2 PIV setup

PIV system was incorporated into the pulsatile flow loop to capture the velocity field in the mid-planes of the sinus and the ascending aorta regions. The tracer particles selected were neutrally buoyant hollow glass microspheres (Sphericel 110P8, Potters Industries LLC., Malvern, PA); with and average diameter of 11.7 μm and density 1100 kg/m^3. The PIV system (Flowmaster, LaVision, Goettingen, Germany) incorporated a double-head Nd:YAG laser (Nano S 30-30 PIV, Litron Lasers, Rugby, England) which generated a pulsed output laser beam (wavelength: 532 nm; max output: 300 mJ; pulse duration: 4ns). For each valve model, the laser sheet was positioned to illuminate two sections of the flow through the laser access window situated on the bath chamber. Laser position 1 was defined as the middle horizontal cross-section of the valve chamber, while laser position 2 illuminated the middle cross-section of the AA model (see Figure 24). The flow in the aorta was measured in two non-aligned planes so that maximum field of view could be attained in both regions of interest. The two sections of the flow were separated by a 10-mm thick stainless-steel block connecting the aorta phantom to the valve chamber. The optical access was blocked for this section of the flow. For each laser position, the camera was placed perpendicular to the laser sheet. Images at these two positions were captured by Imager sCMOS camera (LaVision, Goettingen, Germany), resolution of 2560 × 2160, using AF Micro Nikkor 60 mm lens (Nikon Inc., Melville, NY) and narrow band pass filter (532 ± 10 nm). The camera was used to capture a 62 × 47 mm section of the flow. Image acquisition was performed by dual-channel frame grabber, dual processor 64-bit, and 2.40 GHz computer. Image pairs were captured at 43 phases of the cardiac cycle for each valve model and laser position. For each phase of the cardiac cycle, 100 image pairs were captured. A time filter was applied to remove unsteady laser light reflections by subtracting the minimum intensity. A sliding background was subtracted to overcome the intensity fluctuations in the background. This provided an image with constant background level without affecting the particle signal to be corelated. The vector filed calculated is associated with spurious or false vectors. These spurious vectors were removed using median filter. In order to capture the variations of the average flow field, ensemble averaging was performed on these 100 image pairs at each phase. The Δt between the two image pairs was adjusted in such a way that the maximum average displacement of the particle was approximately 25% of the size of the smallest interrogation window (32 × 32 pixels).

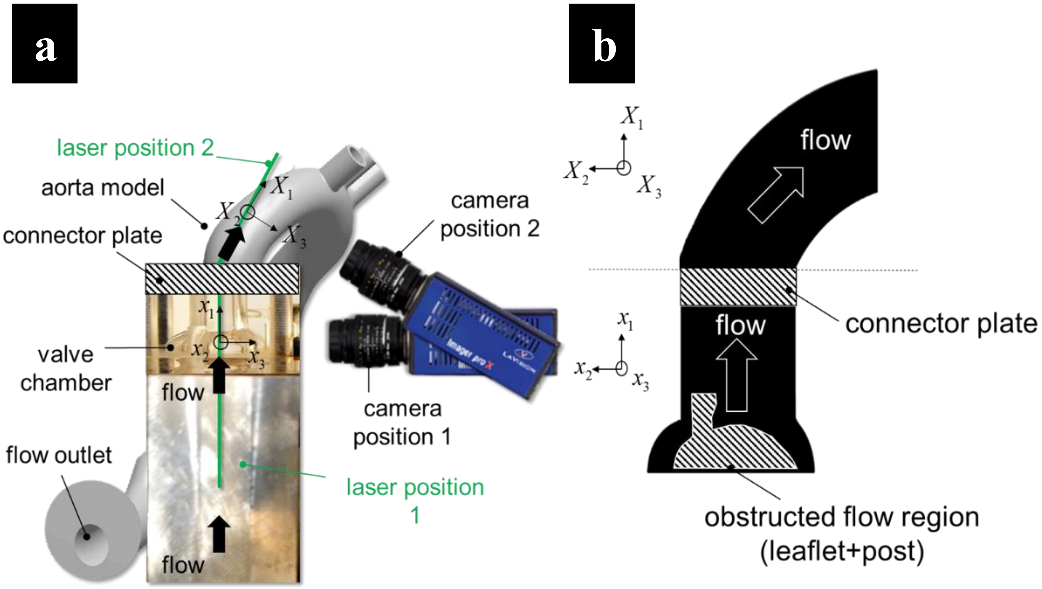

Figure 24: Figure shows flow fields captured and the respective laser and camera positions used to capture (a) camera and laser positions to capture flow characteristics in the proximal and the distal AA region (b) schematic of the flow filed of interest.

The VI allowed to introduce a delay between the opening of the solenoid valve and the trigger that controlled the firing of the laser. This allowed to capture phase-locked PIV images that enabled to measure flow field velocity at specific phases of the cardiac cycle (acceleration, peak systole, deceleration and diastole). Cross-correlation was performed using the commercial PIV software Davis 8.3 (LaVision). A multi-pass scheme was implemented with an initial interrogation window of 64×64 pixels and a final interrogation window of 32×32 pixels. A 50% overlap was introduced between each window to improve spatial resolution and limit in-plane particle loss.

3.5 Uncertainty Analysis

An uncertainty analysis validates the PIV measurements by calculating the difference between actual and the measured values. PIV uncertainty can be divided into two different categories: systemic or bias uncertainties and random uncertainties. Systemic uncertainty or bias uncertainty is a fixed uncertainty associated with a specific system. The bias uncertainty is associated with peak-locking or pixel-locking phenomenon. Pixel locking will occur when the size of the particle image diameter is relatively smaller when compared to the size of the pixel in the camera, causing the velocity to be strongly biased towards the integer-pixel values. This pixel locking effect is unacceptable if the size of the particle image diameter is less than one-pixel unit. To keep the pixel locking effect to a minimum, a widely accepted particle image diameter is of two pixels. Also scientific complementary metal-oxide semiconductor (sCMOS) cameras have small pixel diameter of 5-10 μm. Random uncertainty is variable and can be estimated using repeated measurements. The typical causes of random uncertainty are: noise or cycle-to-cycle variations. This noise can be evaluated by calculating the mean velocity and standard deviation from ensemble averaged date sets. The random uncertainty is inversely proportional to the square root of the number of measurements, thus it is necessary to obtain adequate sample size to reduce the random uncertainty.

3.6 Hemodynamic Characterization

The in-plane instantaneous velocity fields (u: axial component, v: transverse component) obtained by cross-correlation were first filtered to eliminate erroneous velocity vectors and then ensemble-averaged over 100 cardiac cycles to yield an average velocity field ($\overline{u}$: mean axial component, $\bar{v}$: mean transverse component) at each phase. All subsequent analyses were performed in Tecplot 360 (Tecplot Inc., Bellevue, WA). The axial and transverse components of the velocity fluctuation field (u' and v') were obtained from Reynolds decomposition, by subtracting the average velocity components from the instantaneous velocity components:

$$u' = u - \bar{u},$$

$$v' = v - \bar{v},$$

Vorticity, viscous shear stress, Reynolds shear stress and turbulent kinetic energy were used to characterize the flow fields generated by the valve models were evaluated using Tecplot 360 as:

$$\bar{\omega} = \frac{\partial \bar{v}}{\partial x} - \frac{\partial \bar{u}}{\partial y},$$

$$\bar{\tau} = \mu\left(\frac{\partial \bar{u}}{\partial y} + \frac{\partial \bar{v}}{\partial x}\right),$$

$$\tau' = \rho\overline{u'v'},$$

and

$$TKE = \frac{1}{2}\left(\overline{u'^2} + \overline{v'^2}\right),$$

respectively, where ρ is density of blood and μ is the dynamic viscosity, and the overbar denotes an ensemble averaged quantity.

3.7 Left ventricular overload characterization

To calculate the left ventricular overload, a pressure-volume curve was plotted for each valve model. The pressure value for the ejection phase was obtained from the VI, while the corresponding change in the ventricular volume was evaluated from the instantaneous flowrate waveform. The area under the flow rate curve for the ejection phase (Figure 25), was evaluated to measure ventricular volume. This was done by dividing the area into trapezoids with the two parallel sides separated by a time step Δt, thus evaluating the change in the volume. The expression used to evaluate the change in volume:

$$\mathit{\Delta} V = 0.5 \times (Fl_1 + Fl_2) \times \mathit{\Delta} t,$$

where $\mathit{\Delta} V$ is the change in ventricular volume, $\mathit{\Delta} t = t_2 - t_1$, Fl_1 and Fl_2 are the corresponding flowrates at time t_1 and t_2. The sum of all the $\mathit{\Delta} V$ throughout the ejection phase ultimately provides the total ventricular volume

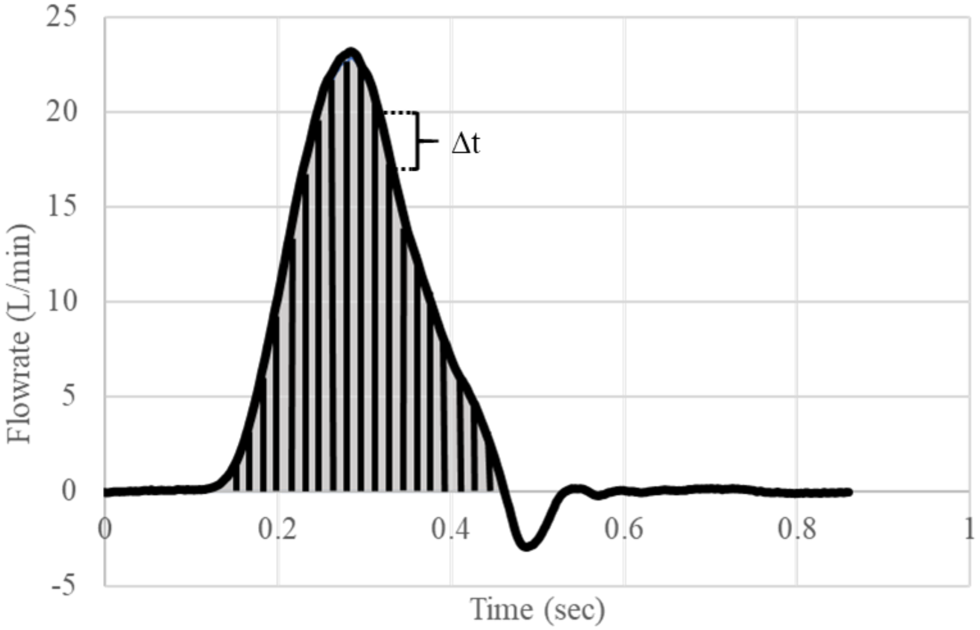

Figure 25: Schematic of the flow rate ejection phase, divided into trapezoidal shaped areas to measure change in the ventricular volume

Once the P-V graph was plotted, the ventricular work was evaluated in Joules by calculating the area under the P-V curve using trapezoidal rule. The expression for work for a change in ventricular volume ΔV :

$$Ventricular\ work = 0.5 \times \left(P_{1(systolic-diastolic)} + P_{2(systolic-diastolic)}\right) \times \Delta V,$$

where $\Delta V = V_2 - V_1$, P_1 and P_2 are the corresponding ventricular pressures at ventricular volume V_1 and V_2

CHAPTER 4:

SPECIFIC AIM 1

The pulsatile flow loop was constructed to mimic the physiological flow in the left side of the human heart. The CO of approximately 5 L/ min was achieved by supplying the compressed air at 25 psi. The aortic and ventricular pressure waveforms matched the physiological values approximately.

4.1 Flowrate waveform

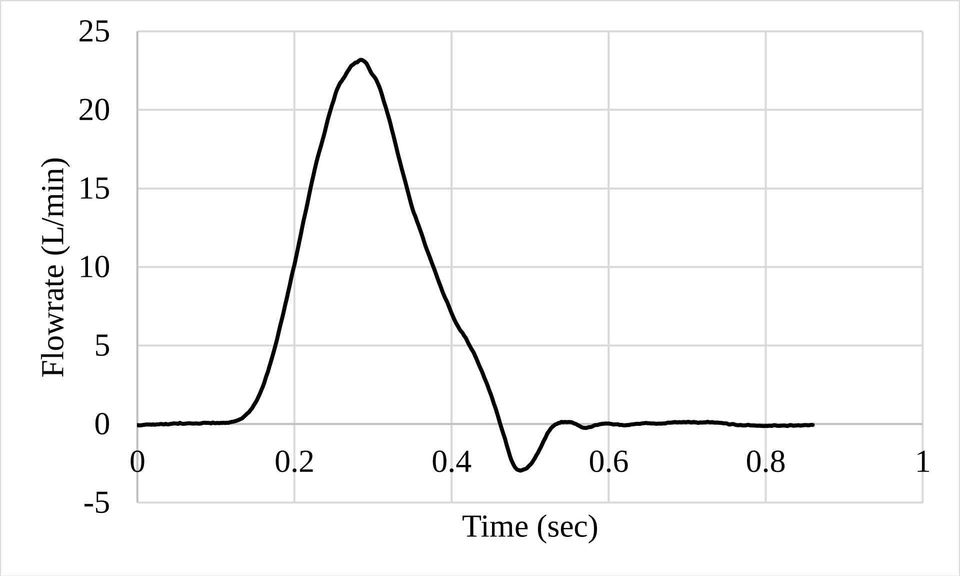

Figure 26: Flowrate waveform generated by the pulsatile flow loop.

The average and the instantaneous flowrate generated by the flow loop was in good agreement with the physiological values [81]. Figure 26 shows the flow rate waveform spanned over one cardiac cycle. The maximum flow rate was 22.7 ± 1.73 L/min while the minimum flow rate was -3.0 ± 0.32 L/min. The flow loop could generate and maintain a physiological CO of 5.0 ± 0.18 L/min.

4.2 Pressure waveforms and mean arterial pressure

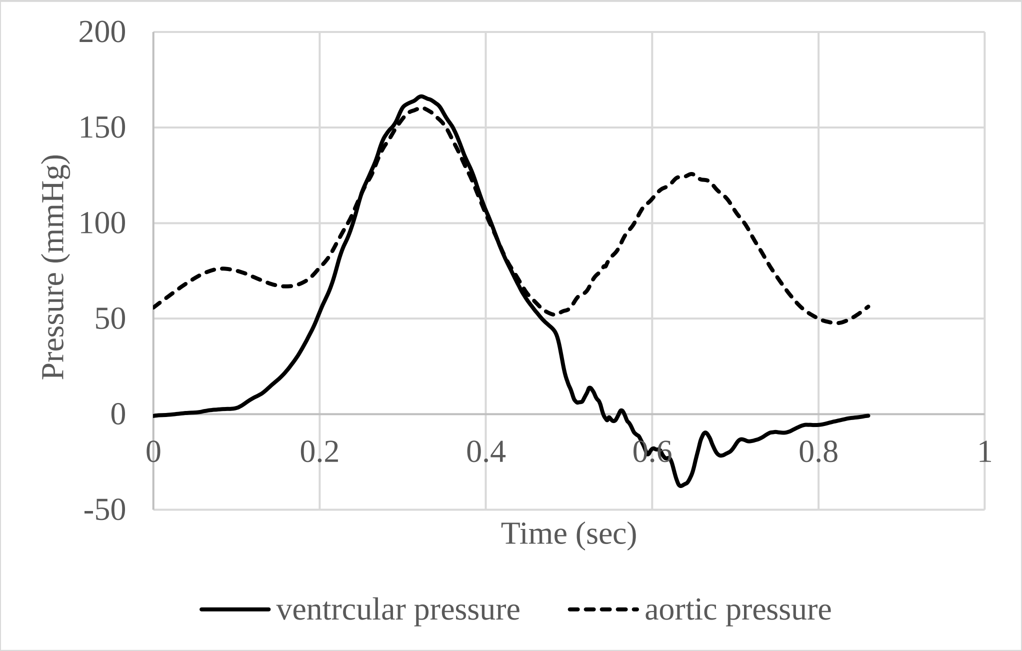

Figure 27: Ventricular and aortic pressure waveform ensemble averaged over 30 cardiac cycles.

Aortic and ventricular pressure waveforms (Figure 27) generated by the flow loop, approximated the physiological pressure waveforms. The systolic ventricular and aortic pressures peaked over 150 mmHg. The ventricular pressure peaked at 163 ± 3.82 mmHg and the aortic pressure was 159 ± 2.91/ 56 ± 1.23 mmHg. However, the mean arterial pressure (MAP) generated by the loop, which is the average arterial pressure over a cardiac cycle [86], was found to lie within the physiological range of 70 to 110 mmHg [85]. The MAP was evaluated as:

$$MAP = diastolic\ pressure + \frac{(systolic\ pressure - diastolic\ pressure)}{3}$$

The MAP generated by the pulsatile flow loop was 90 mmHg.

4.3 Systolic diastolic duration

The systolic duration for the cardiac cycle, can be defined as the interval between the onset of the left ventricular pressure rise and closing of the aortic valve (the icisural notch observed in the aortic pressure waveform) [87]. Based on this definition, the flow loop generated a 0.35 seconds long systole. Thus, the cardiac cycle (0.86 seconds) had a systolic duration of 0.35 seconds which implied a diastolic duration of 0.51 seconds. This resulted in a systolic diastolic (S/D) ratio of 0.7 which lies within the clinically measured range of S/D ratio [88]

Although the ventricular and aortic pressure waveforms were an approximate of the physiological waveforms, the flow loop could still generate a flowrate waveform and a cardiac output which was in good agreement with physiological values. The MAP and S/D ratio were well within its defined physiological range. These results implicate that the flow loop could generate flow within the physiological parameters

4.4 Discussion

The target of this aim was to construct and validate the pulsatile flow loop that could replicate physiological flow conditions in the aortic valve and AA. The flow loop was tuned by adjusting the compressed air that enabled to generate flow within the physiological range of -5 to 20 L/min and a CO of approximately 5 L/min. The aortic pressure was adjusted to match the physiological values by altering the resistance and compliance, but the aortic pressure peak showed a higher value compared to the physiological waveform even after altering the compliance and the resistance of the loop. MAP calculated from the aortic pressures values, however lied within the physiological range of 70 and 110 mmHg. The S/D ratio also was well within its physiological limits. Thus, the flow loop was able to generate a flow rate, MAP and cardiac cycle with S/D ratio that lied within the physiological parameters

CHAPTER 5:

SPECIFIC AIM 2

This aim characterized the effect of valvular stenosis on flow dynamics in the proximal and the distal ascending aorta (PAA and DAA, respectively). The pulsatile flow loop and PIV setup described in sections 3.1 and 0 respectively, were used to capture the ensemble-averaged velocity fields in the region of interest. A normal TAV (nTAV) and two calcified TAVs (mTAV and sTAV) were used to quantify the impact of the degree of stenosis on the instantaneous ensemble-averaged velocity, vorticity, turbulent kinetic energy, viscous shear stress (VSS) and Reynolds shear stress (RSS) fields. The flow was investigated during the acceleration phase, at peak systole, during the deceleration phase and early diastolic phase.

5.1 Velocity Field

Ensemble-averaged velocity fields at four phases of the cardiac for all three valve models are shown in Figure 28. During the acceleration phase, all the valve models generated forward flow with distinctive jet structures in the proximal ascending aorta (PAA) and the distal ascending aorta (DAA). In the PAA, the nTAV generated a wide symmetric low velocity jet, while the reduced valve orifice of the mTAV and sTAV caused an increase jet velocity in the PAA. The sTAV resulted in an abnormally high velocity jet in the PAA, while relatively low velocities were observed in the distal region for all the valve models during this phase. A high velocity jet in PAA and a low velocity jet in the DAA was observed for the sTAV. This variation in the velocity existing amongst the two regions (proximal and distal) downstream of the sTAV, can be reasoned with the high velocity jet falling out of the plane of observation in the DAA. At peak systole, the nTAV generated lowest velocity of all the three valve models. The mTAV and sTAV generated a 37% and 117 % increase in velocity, respectively when compared to nTAV. A drop in the velocity was observed during the deceleration phase downstream of the nTAV, while the mTAV and sTAV continued to demonstrate high velocity jets in the DAA and the PAA, respectively. During early diastole, the valve shut close and no significant flow structures were observed in any valve model. The fluid velocities remained close to zero during this phase.

Table 2: Peak velocity data in the AA during the acceleration phase, at peak systole, during the deceleration phase and during early diastole

PAA	nTAV	mTAV	sTAV
Acceleration	1.2 m/s	1.8 m/s	4.16 m/s
Peak systole	2.3 m/s	3.3 m/s	5.0 m/s
Deceleration	1.9 m/s	2.09 m/s	3.19 m/s
Diastole	0.16 m/s	0.30 m/s	0.33 m/s

DAA	nTAV	mTAV	sTAV
Acceleration	1.15 m/s	1.69 m/s	0.9 m/s
Peak systole	1.7 m/s	2.98 m/s	1.04 m/s
Deceleration	1.39 m/s	2.28 m/s	0.87 m/s
Diastole	0.06 m/s	0.41 m/s	0.22 m/s

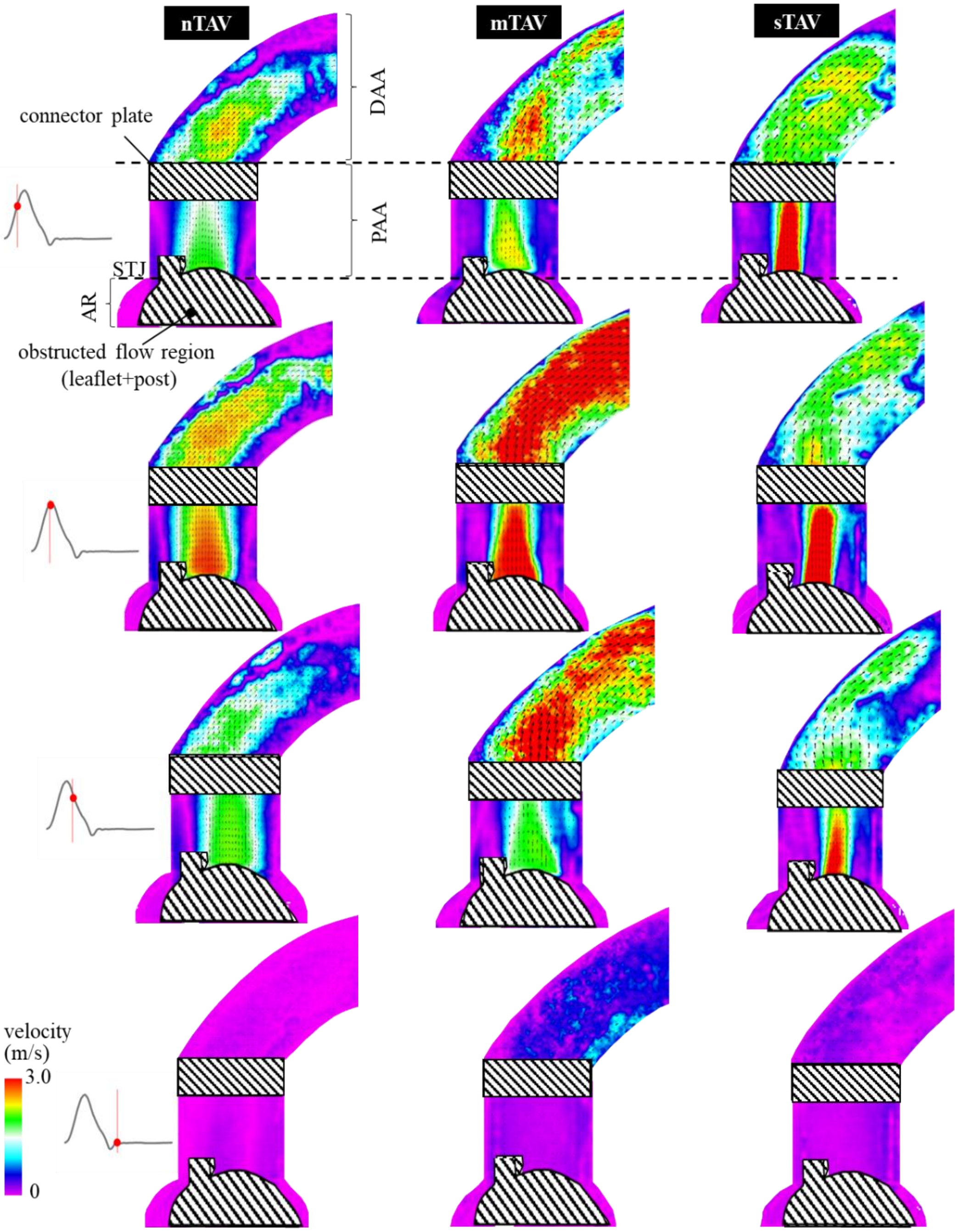

Figure 28: Ensemble-averaged velocity fields captured for nTAV, mTAV and sTAV valve models (left to right in order) in the PAA (proximal ascending aorta) and the DAA (distal ascending aorta) region.

5.2 Vorticity Field

Figure 29 shows the ensemble-averaged out-of-plane vorticity fields at four phases of the cardiac cycle for all three valve models. The red and blue colors indicate counterclockwise and clockwise vorticity, respectively. The highest magnitude of vorticity was found along the edges of the jet emanating from the valves. All three valve models produced counterclockwise (positive rotation) vorticity near the convexity of the AA, while clockwise (negative rotation) vorticity was observed near the concavity. The nTAV model generated the lowest magnitude of vorticity during the acceleration phase, when compared to the stenosed valve models. This trend continued at peak systole, as the mTAV and sTAV had vorticity magnitude 56% and 200% more than the nTAV. The nTAV model exhibited shear layers around the edge of the orifice jet that were both symmetrical and parallel to the axis of the valve in the PAA and the DAA. In contrast, the mTAV and sTAV generated asymmetric vorticity patterns. The deceleration phase was characterized by the same vorticity patterns as those observed at peak systole but with reduced magnitude. Vorticity magnitude was relatively low at diastole for all the three valve models, when compared with other phases.

Table 3: Ensemble-averaged vorticity data captured during the acceleration phase, at peak systole, during the deceleration phase and during early diastole

PAA	nTAV	mTAV	sTAV
Acceleration	498 s^{-1}	870 s^{-1}	2795 s^{-1}
Peak systole	1165 s^{-1}	1816 s^{-1}	3493 s^{-1}
Deceleration	578 s^{-1}	944 s^{-1}	2479 s^{-1}
Diastole	115.8 s^{-1}	253.4 s^{-1}	435 s^{-1}

DAA	nTAV	mTAV	sTAV
Acceleration	519 s^{-1}	702 s^{-1}	724 s^{-1}
Peak systole	732 s^{-1}	1176 s^{-1}	826 s^{-1}
Deceleration	542 s^{-1}	656 s^{-1}	673 s^{-1}
Diastole	107 s^{-1}	284 s^{-1}	270 s^{-1}

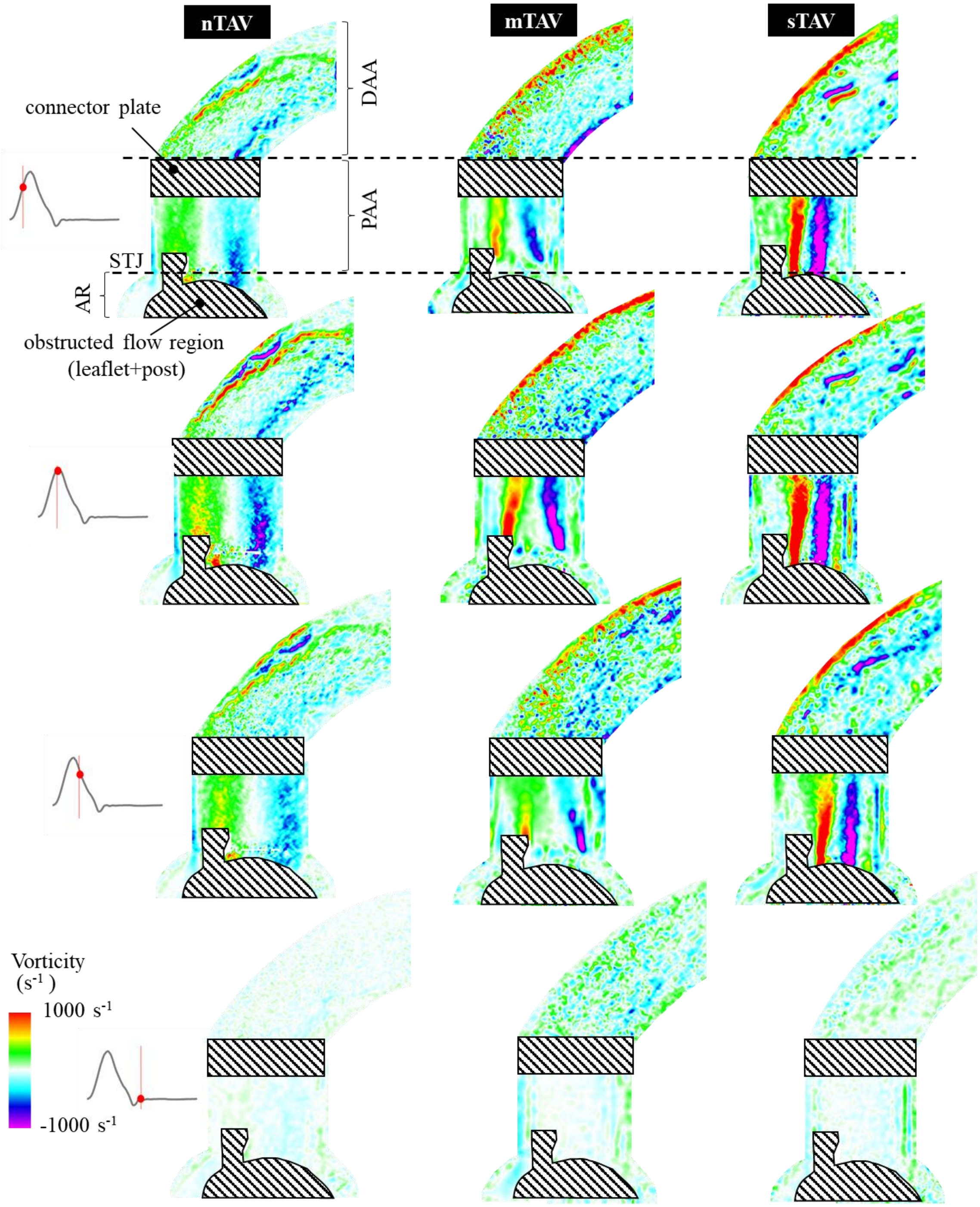

Figure 29: Ensemble-averaged vorticity fields captured for nTAV, mTAV and sTAV valve models (left to right in order) in the PAA (proximal ascending aorta) and the DAA (distal ascending aorta) region.

5.3 Viscous and Reynolds Shear Stress Fields

The distributions of viscous shear stress (VSS) at four phases of the cardiac cycle for all three valve models is shown in Figure 30. The VSS plots exhibit some similarities with the vorticity plots, as the regions of maximum shear stress are found along the edges of the jet. This phenomenon is expected as the highest velocity gradients are found near the regions of flow separation. Low VSS magnitude was associated with nTAV throughout the cardiac cycle. However, a noticeable difference between the VSS fields was observed amongst the stenosed valves during the acceleration phase. Elevated VSS dominated the DAA and PAA downstream of the mTAV and sTAV, respectively. A similar trend was observed at peak systole, but with higher VSS magnitude. The reduced valve orifice produced by the mTAV and sTAV led to the narrowing of the jet, causing a 150% increase in VSS for mTAV and 216% increase for sTAV, relative to the nTAV. During the deceleration phase, regions of high VSS continued to occupy the mTAV DAA and sTAV PAA. VSS values were low for all valve models during diastole.

Table 4: Ensemble-averaged VSS data captured during the acceleration phase, at peak systole, during the deceleration phase and during early diastole.

PAA	nTAV	mTAV	sTAV
Acceleration	0.21 N/m^2	0.44 N/m^2	2.8 N/m^2
Peak systole	1.04 N/m^2	2.6 N/m^2	3.2 N/m^2
Deceleration	0.41 N/m^2	0.43 N/m^2	2.0 N/m^2
Diastole	0.01 N/m^2	0.03 N/m^2	0.08 N/m^2

DAA	nTAV	mTAV	sTAV
Acceleration	0.23 N/m^2	0.31 N/m^2	0.66 N/m^2
Peak systole	0.54 N/m^2	1.12 N/m^2	1.02 N/m^2
Deceleration	0.19 N/m^2	0.39 N/m^2	0.56 N/m^2
Diastole	0.02 N/m^2	0.017 N/m^2	0.11 N/m^2

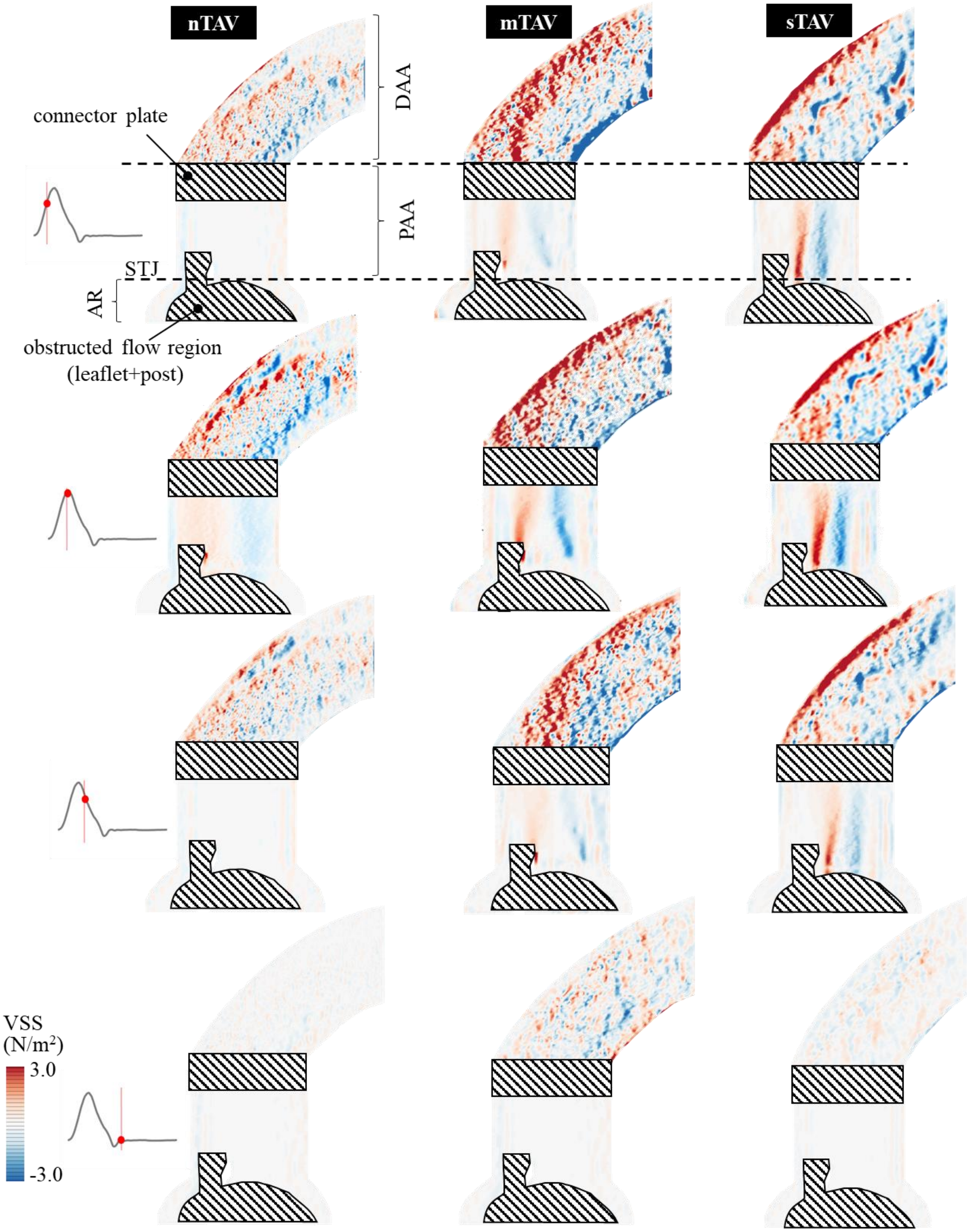

Figure 30: Ensemble-averaged VSS fields captured for nTAV, mTAV and sTAV va
models (left to right in order) in the PAA (proximal ascending aorta) and the DAA (
ascending aorta) region.

Figure 31 shows the Reynolds shear stress (RSS) fields for all three valve models at four phases of the cardiac cycle. Irrespective of the degree of stenosis, the two stenosed valve models generated peak RSS values two-orders of magnitude greater than the peak VSS, thus it can be deduced that the flow was dominated by turbulent stresses. These turbulent effects were more prominent in the wake of the valve leaflets where the turbulence and velocity fluctuations attained their maximum. During the acceleration phase, significant differences were observed, nTAV had relatively low RSS magnitude throughout the AA, whereas the convexity of mTAV DAA and sTAV PAA featured 92% and 267% increase in RSS magnitude, respectively when compared with the nTAV. At peak systole, nTAV had a maximum RSS value of 165 N/m^2 while mTAV and sTAV showed a 39 % and 200 % increase, respectively. During the deceleration phase, high RSS regions were still prevalent in the mTAV DAA, while very low velocity fluctuations were measured throughout the nTAV AA. The diastolic phase did not exhibit any substantial difference in RSS between the valve models and was characterized with very low RSS magnitude for all the valve models, when compared to other phases.

Table 5: RSS data captured during the acceleration phase, at peak systole, during the deceleration phase and during early diastole

PAA	nTAV	mTAV	sTAV
Acceleration	85 N/m^2	163 N/m^2	307 N/m^2
Peak systole	165 N/m^2	230 N/m^2	502 N/m^2
Deceleration	108 N/m^2	120 N/m^2	250 N/m^2
Diastole	3.24 N/m^2	3.0 N/m^2	5.4 N/m^2

DAA	nTAV	mTAV	sTAV
Acceleration	86 N/m^2	225 N/m^2	70 N/m^2
Peak systole	98 N/m^2	203 N/m^2	105 N/m^2
Deceleration	71.6 N/m^2	170 N/m^2	82 N/m^2
Diastole	2.15 N/m^2	5.2 N/m^2	4.3 N/m^2

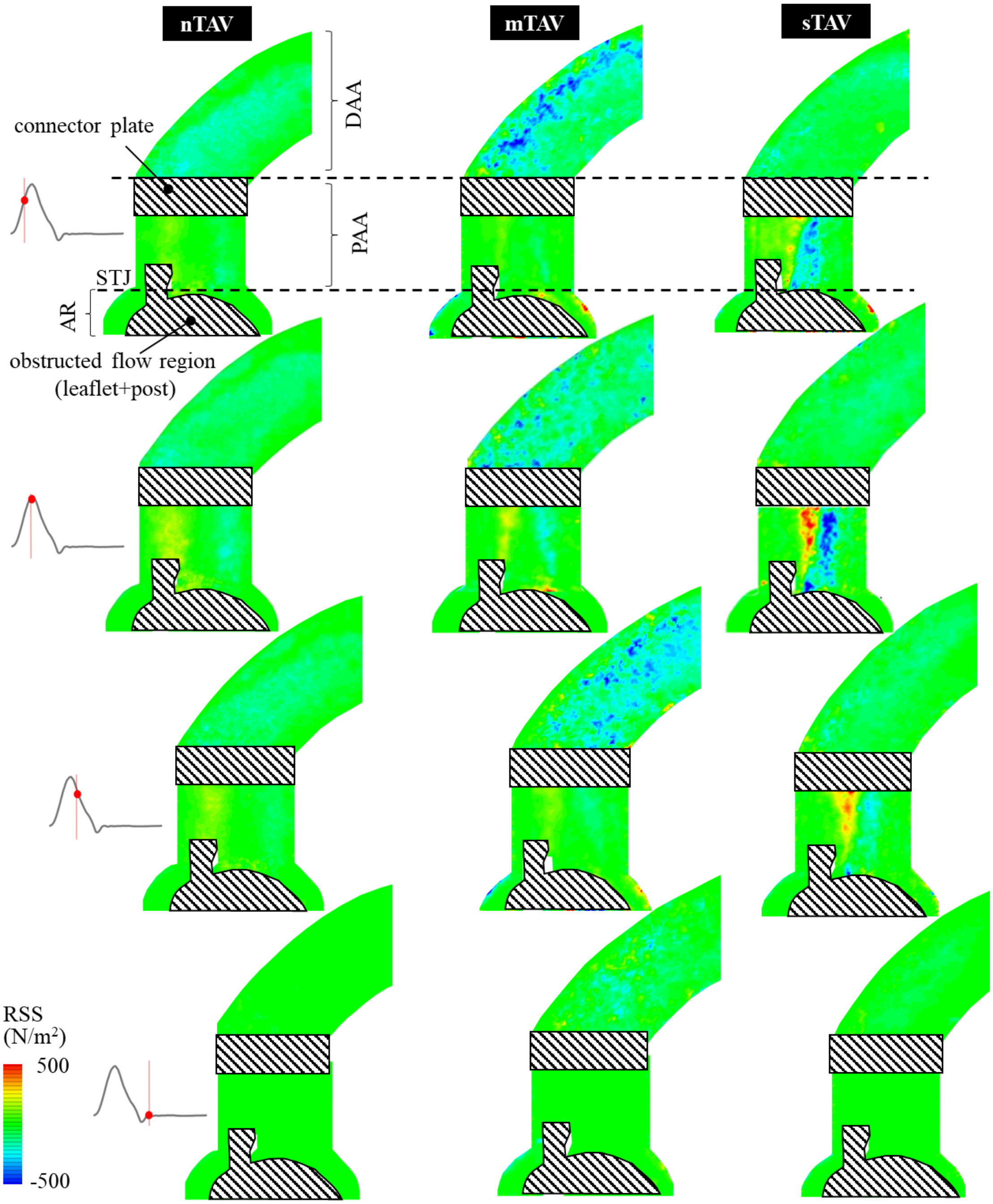

Figure 31: Ensemble-averaged RSS fields captured for nTAV, mTAV and sTAV valve models (left to right in order) in the PAA (proximal ascending aorta) and the DAA (distal ascending aorta) region.

5.4 Turbulent Kinetic Energy

Turbulent Kinetic Energy (TKE) fields at four phases of the cardiac cycle for all three valve models are shown in Figure 32. Following the trend observed with the RSS distribution, the nTAV resulted in the lowest TKE. A sharp increase in TKE was observed near the convexity of the mTAV DAA during the acceleration phase. The sTAV model showed similar characteristics in the PAA. While valvular stenosis generated up to 300% increase in TKE relative to the nTAV, at peak systole; the affected region depended upon the degree of stenosis. The mTAV caused 113 % increase in DAA relative to nTAV. sTAV generated high TKE values close to the valve leaflets in the PAA, a 286 % increase, when compared to nTAV. During the deceleration phase, the stenosed valves continued to generate high TKE, while low TKE was observed for all the valve models during diastole.

Table 6: TKE data captured during the acceleration phase, at peak systole, during the deceleration phase and during diastole.

PAA	nTAV	mTAV	sTAV
Acceleration	0.59 m^2/s^2	0.96 m^2/s^2	1.02 m^2/s^2
Peak systole	1.45 m^2/s^2	1.2. m^2/s^2	5.6 m^2/s^2
Deceleration	0.51 m^2/s^2	0.5 m^2/s^2	1.44 m^2/s^2
Diastole	0.02 m^2/s^2	0.02 m^2/s^2	0.05 m^2/s^2

DAA	nTAV	mTAV	sTAV
Acceleration	0.33 m^2/s^2	1.31 m^2/s^2	0.37 m^2/s^2
Peak systole	0.43 m^2/s^2	3.2. m^2/s^2	0.84 m^2/s^2
Deceleration	0.31 m^2/s^2	0.97 m^2/s^2	0.34 m^2/s^2
Diastole	0.017 m^2/s^2	0.18 m^2/s^2	0.13 m^2/s^2

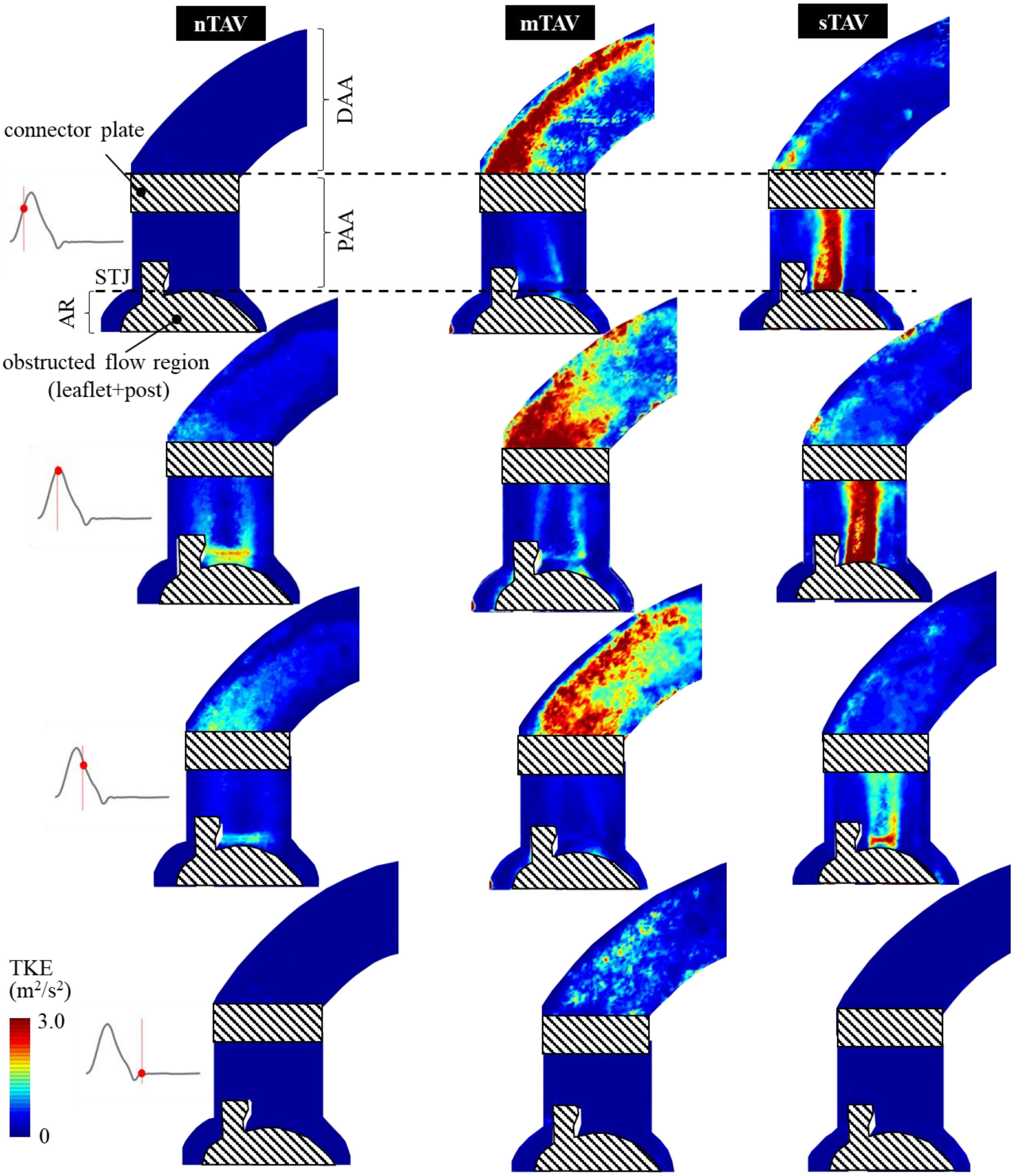

Figure 32: Ensemble-averaged TKE fields captured for nTAV, mTAV and sTAV valve models (left to right in order) in the PAA (proximal ascending aorta) and the DAA (distal ascending aorta) region.

5.5 Effective orifice area

The effective orifice area for all three valve models were calculated using the Gorlin equation mentioned in 1.4.2.1 *Diagnosis*. The calculated EOA for all the three valve models were 2.21 cm^2 for the nTAV model (normal TAV), 1.18 cm^2 for the mTAV model (moderately stenosed valve model) and 0.69 cm^2 for sTAV (severely stenosed valve model).

The effective orifice area calculated from the PIV images for the nTAV model was 2.01 cm^2, for the mTAV model was 1.28 cm^2 and for the sTAV was 0.72 cm^2. The area was calculated at the location of vena-contracta for all the three valve models. The effective orifice area was evaluated from the velocity jets observed in the velocity field obtained from PIV.

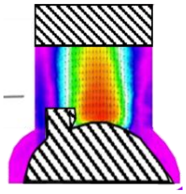
nTAV

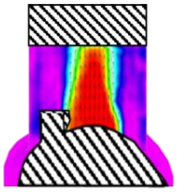
mTAV

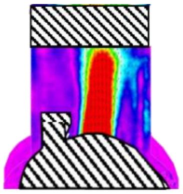
sTAV

The values of effective orifice are calculated for all the three valve models were within the range defined for calcific aortic stenosis by AHA statistics.

5.6 Discussion

The goal of this aim was to study the effect of valvular stenosis on aorta hemodynamics by implementing PIV to characterize the flow downstream of the normal aortic valve model nTAV, and its stenosed counterparts, mTAV and sTAV. In this aim, the hemodynamics in the proximal and the distal region of the AA, across the three valve models were compared using ensemble averaged velocity, vorticity, viscous shear stress, Reynolds shear stress and turbulent kinetic energy fields at acceleration, peak systole, deceleration and early diastolic phases of the cardiac cycle.

This study used a common aorta phantom for all the three valve models which allowed to evaluate and seclude the impact of aortic valve stenosis on aorta hemodynamics. The reduced valve orifice for the stenosed valve models generated hemodynamic alterations which were characterized by elevated jet velocities. The sTAV with the highest degree of stenosis was associated with the maximum jet velocity out of the two stenosed valve models. This observation implies that the magnitude of jet velocity was highly dependent on the severity of stenosis. These findings were in line with the previous invitro, and computational studies that studied the impact of stenosis over valvular flow [63], [64], [89]. The nTAV model showed a jet like flow in the ascending aorta. However, the flow was more of three dimensional in case of stenosed valve models. This is observed in case of sTAV model where the three-dimensional characteristic of the jet caused it to fall out of the plane of the measurement. The dependence of hemodynamic alterations over the degree of stenosis was observed for all the flow metrics. Vorticity and VSS magnitudes were relatively higher downstream of the stenosed valve models, when compared to the healthy one. Regions of elevated VSS were present in both the convexity and concavity of the AA. This suggested that the regions of elevated VSS corresponded to the symmetric dilation pattern associated with TAV AA. High VSS was prevalent in the stenosed valve flow filed not only for the peak systole but also during the acceleration and the deceleration phase of the cardiac cycle. This highlight the fact that the aortic wall was exposed to higher VSS for a longer duration in case of stenosed valve models, when compared to normal valve.in a cardiac cycle. The degree dependent characteristic of VSS were also found to match the findings of the previous MRI and invitro studies [64], [90], [91]

The intensity of fluctuations in the flow filed was characterized in terms of TKE and RSS which are both evaluated using fluctuating components of velocities. Both TKE and RSS were dependent on the severity of stenosis, with the maximum values associated with the severely stenosed valve.

The effective orifice area calculated using Gorlin equation for this study approximated the effective orifice area measured from the flow images, captured using particle image velocimetry. This implies that stenosed valve models designed using commissural fusion could generate stenosis with effective orifice area equal to the values calculated mathematically. These calculated and measured effective orifice areas for all the three valve models were within the clinically defined physiological ranges.

Overall these results have demonstrated that valvular stenosis significantly altered the flow downstream of the stenosed valves in the AA when compared to normal aortic valve. The results also show that these flow abnormalities were concentrated in the regions prone to dilation in CAS aortopathy. In vivo studies have associated elevated wall shear stress in the AA with aortic stenosis using magnetic resonance imaging and thus support the finding of this study [90], [91]. Shear stresses alterations in the AA can result in abnormal biological responses from aorta wall endothelium leading to progressive tissue alterations, aorta wall remodeling with possible dilation and dissection. In vivo studies subjecting endothelial cells to chronic shear stress support this claim [92]. These observations provide increasing evidence for the involvement of hemodynamics in the stenosis associated aortopathy. These results isolate the impact of CAS on aorta flow in a non-dilated compliant silicon aorta model. The results demonstrate the impact of CAS on AA hemodynamics in regions prone to dilations providing more evidence to the existence of hemodynamic pathway in CAS aortopathy. These hemodynamic alterations could cause adverse biological response from the aortic wall leading a positive feedback cycle and accelerating disease progression. These observations suggest that there is a need to further investigate the effects of flow abnormalities on aorta wall biology. Thus histopathological studies should be performed in future to assess the impact of these hemodynamic alterations on aortic tissue.

CHAPTER 6:

SPECIFIC AIM 3

This aim evaluated the effect of valvular stenosis on left ventricular (LV) function. Due to impaired leaflet motion and narrowed valvular orifice, the blood flow is restricted. To maintain the same CO, the left ventricle must perform additional work. This overload imposed by a stenosed valve on the left ventricle is evaluated in this aim.

6.1 Ventricular work

The pressure-volume (PV) graphs (Figure 33) were plotted and the left ventricular work for each valve model was calculated by evaluating the area under its associated PV curves.

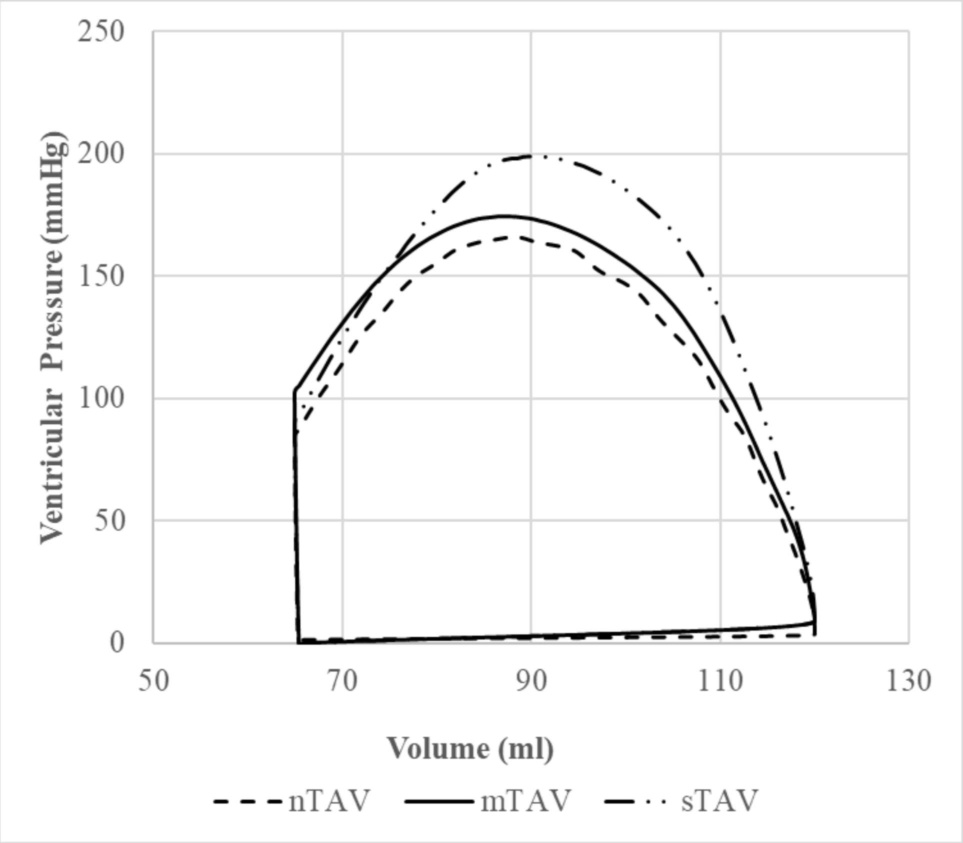

Figure 33: Figure shows the pressure-volume graphs for all three valve models: nTAV, mTAV and sTAV.

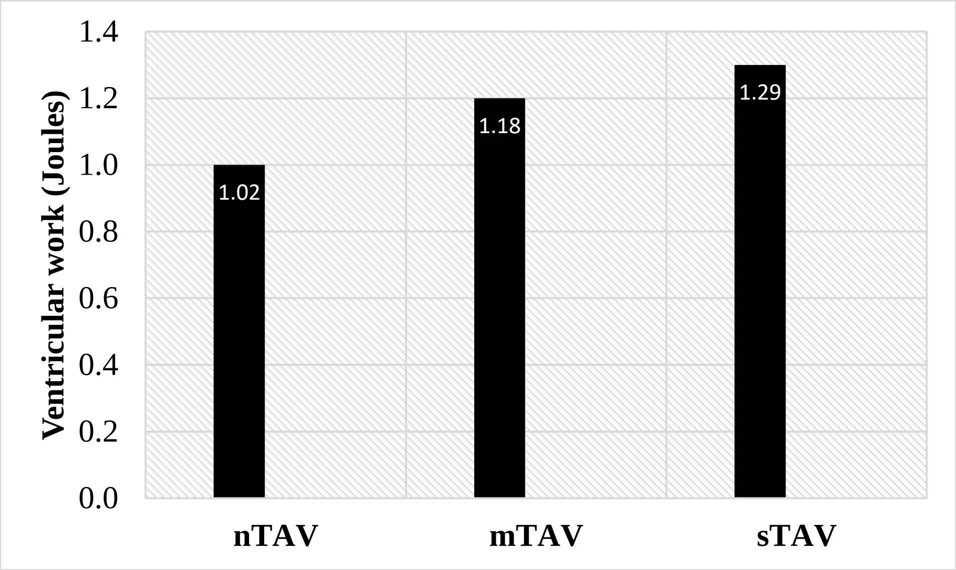

Figure 34: Bar graph showing left ventricular work associated with each of the valve models: nTAV, mTAV and sTAV

An increase in the ventricular pressure was observed for each of the stenosed valve models. The peak systolic pressure for mTAV was approximately 175 mmHg while that for sTAV was around 200 mmHg.

As shown in the Figure 34, the nTAV was associated the lowest amount of ventricular work. The introduction of valvular stenosis caused ventricular overload of 16% for the mTAV and 27 % for the sTAV, when compared with the normal valve.

6.2 Discussion

This aim evaluated the amount of work, the LV does to maintain the physiological cardiac output in case of valvular stenosis. In CAS, the aortic valve undergoes structural changes in the form of leaflet stiffening, reduced valve orifice and impaired leaflet motion generating obstruction to the blood flowing in to the aorta. To overcome this obstruction and maintain the CO, the ventricle is subjected to an overload. In this study valvular stenosis, imposed up to 27 % of overload on the left ventricular. The amount of ventricular overload increased with the severity of stenosis. Clinical studies have shown ventricular overload to increase LV mass and wall thickness, causing LV hypertrophy and heart failure [93]. Thus, the results of this aim demonstrate the association of aortic stenosis with LV overload, and its impact on LV function in a degree dependent manner.

CHAPTER 7:

CONCLUSION

CAS is a slow progressive disease characterized by reduced valve orifice and impaired leaflet motion of the aortic valve and has been associated with aortopathy and left ventricular dysfunction. This in vitro study isolated the impact of the degree of valvular stenosis on left ventricular workload and aorta hemodynamics. The results of this study demonstrated 1) altered hemodynamics in the aorta in case of stenosed valves, 2) excess ventricular workload imposed due valvular stenosis. Stenosis resulted in regions of elevated velocity, shear stress and turbulence at locations prone to dilation in the aorta, providing additional evidence to the hemodynamic theory of CAS associated aortopathy. The excess ventricular work in case of the stenosed valves explain the association of ventricular hypertrophy with aortic stenosis. The findings of this study thus explain the susceptibility of CAS patients to aortopathy and heart failure.

CHAPTER 8:

LIMITATIONS

This study had considerable limitations that requires attention. The PIV setup allowed to capture the flow in 2-dimensions, while a 3-dimensional flow field would have provided better understanding of the flow structures downstream of the aortic valve. This limitation might explain the drastic change in the velocity amongst the proximal and distal sections of sTAV aorta, since the high velocity jet was oriented outside the span of the 2-dimensional measurement plane in the distal region. However, this did not halter the study from demonstrating significant flow differences that existed downstream of the three valve models. The near wall flow characteristics could not be characterized using PIV due to non-homogenous seeding near the wall as the particles tend to move away from the wall. The aortic and ventricular pressures generated by the flow loop approximated the physiological values. This can be linked to the insufficiency of the flow loop to mimic the systemic compliance and resistance. The cardiac output and the instantaneous flow rate generated by the flow loop, however were well within the physiological limits. Porcine aortic valve models were used in this study and valvular stenosis was modelled using commissural fusion. The reliability of this method to mimic stenosis was questionable because the artificial reduction created in the valve orifice to model stenosis was heavily idealized based on trial and error. However, the downstream flow velocity in the aorta and the transvalvular pressure gradient obtained from the PIV post processing and pressure transducers respectively, lied well within the AHA statistics for aortic stenosis.

BIBLIOGRAPHY

[1] "MBBS Medicine (Humanity First): Heart muscles,as a pump and functions of valves." [Online]. Available: http://medicinembbs.blogspot.com/2011/02/heart-musclesas-pump-and-functions-of.html. [Accessed: 27-Nov-2017].

[2] J.-L. Vincent, "Understanding cardiac output.," *Crit. Care*, vol. 12, no. 4, p. 174, 2008.

[3] "Chordae tendineae - Location, Function and Pictures." [Online]. Available: https://www.knowyourbody.net/chordae-tendineae.html. [Accessed: 26-Feb-2018].

[4] "Left Ventricle." [Online]. Available: https://www.liverpool.ac.uk/~trh/local_html/heartdisease/left_ventricle.htm. [Accessed: 25-Feb-2018].

[5] "V. Angiology. 4b. The Heart. Gray, Henry. 1918. Anatomy of the Human Body." [Online]. Available: http://www.bartleby.com/107/138.html. [Accessed: 26-Feb-2018].

[6] "Bio 100: Heart Anatomy." [Online]. Available: http://www.biosbcc.net/b100cardio/htm/heartant.htm. [Accessed: 25-Feb-2018].

[7] R. B. Hinton and K. E. Yutzey, "Heart valve structure and function in development and disease.," *Annu. Rev. Physiol.*, vol. 73, pp. 29–46, 2011.

[8] Garg Shivani, "Aortic Valve Anatomy: Overview, Gross Anatomy, Microscopic Anatomy." [Online]. Available: https://emedicine.medscape.com/article/1922899-overview#a1. [Accessed: 27-Nov-2017].

[9] J. A. Stella and M. S. Sacks, “On the Biaxial Mechanical Properties of the Layers of the Aortic Valve Leaflet,” *J. Biomech. Eng.*, vol. 129, no. 5, p. 757, Oct. 2007.

[10] M. Rozeik, D. Wheatley, and T. Gourlay, “The aortic valve: structure, complications and implications for transcatheter aortic valve replacement,” *Perfusion*, vol. 29, no. 4, pp. 285–300, Jul. 2014.

[11] I. Vesely and R. Noseworthy, “MICROMECHANICS OF THE FIBROSA AND THE VENTRICULARIS IN AORTIC VALVE LEAFLETS,” *J. Biomechics*, vol. 25, no. 1, pp. 101–113, 1992.

[12] E. U. S. of M. Shivani Garg, MD, MBBS Fellow, Department of Rheumatology, “Aortic Valve Anatomy.”

[13] M. M. Rozeik, D. J. Wheatley, and T. Gourlay, “The aortic valve: Structure, complications and implications for transcatheter aortic valve replacement,” *Perfusion (United Kingdom)*. 2014.

[14] H.-L. Leo, E. Simon, J. Carberry, S.-C. Lee, and A. P. Yoganathan, “A Comparison of Flow Field Structures of Two Tri-Leaflet Polymeric Heart Valves,” *Ann. Biomed. Eng.*, vol. 33, no. 4, pp. 429–443, 2005.

[15] B. R. Lindman *et al.*, “Calcific aortic stenosis,” *Nat. Rev. Dis. Prim.*, p. 16006, 2016.

[16] R. V. Freeman and C. M. Otto, “Spectrum of calcific aortic valve disease: Pathogenesis, disease progression, and treatment strategies,” *Circulation*, vol. 111, no. 24, pp. 3316–3326, 2005.

[17] N. M. Rajamannan and C. M. Otto, “Targeted Therapy to Prevent Progression of Calcific Aortic Stenosis,” *Circulation*, vol. 110, no. 10, pp. 1180–1182, Sep. 2004.

[18] “Aortic valve stenosis - Symptoms and causes - Mayo Clinic.” [Online]. Available: https://www.mayoclinic.org/diseases-conditions/aortic-stenosis/symptoms-causes/syc-20353139. [Accessed: 23-Jan-2018].

[19] K. E. Yutzey *et al.*, “Brief Review Calcific Aortic Valve Disease A Consensus Summary From the Alliance of Investigators on Calcific Aortic Valve Disease,” pp. 2387–2394, 2014.

[20] B. A. Carabello and W. J. Paulus, “Aortic stenosis,” *Lancet*, vol. 373, no. 9667, pp. 956–966, 2009.

[21] B. R. Lindman *et al.*, “Calcific aortic stenosis,” *Nat. Rev. Dis. Prim.*, vol. 2, p. 16006, Mar. 2016.

[22] A. S. Go *et al.*, “Executive summary: heart disease and stroke statistics--2013 update: a report from the American Heart Association.,” *Circulation*, vol. 127, no. 1, pp. 143–52, Jan. 2013.

[23] S. Coffey, B. Cox, and M. J. A. Williams, “The Prevalence, Incidence, Progression, and Risks of Aortic Valve Sclerosis: A Systematic Review and Meta-Analysis,” *J. Am. Coll. Cardiol.*, vol. 63, no. 25, pp. 2852–2861, Jul. 2014.

[24] V. T. Nkomo, J. M. Gardin, T. N. Skelton, J. S. Gottdiener, C. G. Scott, and M. Enriquez-Sarano, “Burden of valvular heart diseases: a population-based study.,” *Lancet (London, England)*, vol. 368, no. 9540, pp. 1005–11, Sep. 2006.

[25] G. W. Eveborn, H. Schirmer, G. Heggelund, P. Lunde, and K. Rasmussen, “The evolving epidemiology of valvular aortic stenosis. the Tromsø study.,” *Heart*, vol. 99, no. 6, pp. 396–400, Mar. 2013.

[26] E. J. Benjamin *et al.*, “Heart Disease and Stroke Statistics—2017 Update: A

Report From the American Heart Association," *Circulation*, 2017.

[27] A. Vahanian *et al.*, "Guidelines on the management of valvular heart disease (version 2012): The Joint Task Force on the Management of Valvular Heart Disease of the European Society of Cardiology (ESC) and the European Association for Cardio-Thoracic Surgery (EACTS)," *Eur. Heart J.*, vol. 33, no. 19, pp. 2451–2496, Oct. 2012.

[28] M. J. Budoff *et al.*, "Reproducibility of CT measurements of aortic valve calcification, mitral annulus calcification, and aortic wall calcification in the multi-ethnic study of atherosclerosis.," *Acad. Radiol.*, vol. 13, no. 2, pp. 166–72, Feb. 2006.

[29] H. Baumgartner *et al.*, "Echocardiographic Assessment of Valve Stenosis: EAE/ASE Recommendations for Clinical Practice," *J. Am. Soc. Echocardiogr.*, vol. 22, no. 1, pp. 1–23, Jan. 2009.

[30] M. J. Czarny and J. R. Resar, "Diagnosis and management of valvular aortic stenosis.," *Clin. Med. Insights. Cardiol.*, vol. 8, no. Suppl 1, pp. 15–24, 2014.

[31] R. O. American College of Cardiology/American Heart Association Task Force on Practice Guidelines *et al.*, "ACC/AHA 2006 guidelines for the management of patients with valvular heart disease: a report of the American College of Cardiology/American Heart Association Task Force on Practice Guidelines (writing committee to revise the 1998 Guidelines for the Management of Patients With Valvular Heart Disease): developed in collaboration with the Society of Cardiovascular Anesthesiologists: endorsed by the Society for Cardiovascular Angiography and Interventions and the Society of Thoracic Surgeons.,"

Circulation, vol. 114, no. 5, pp. e84-231, Aug. 2006.

[32] B. Grimard, M. Larson, S. Clinic, and F. Augustine, “Aortic Stenosis: Diagnosis and Treatment.”

[33] “Valvuloplasty - Overview - Mayo Clinic.” [Online]. Available: https://www.mayoclinic.org/tests-procedures/valvuloplasty/gnc-20302461. [Accessed: 26-Feb-2018].

[34] P. Pibarot and J. G. Dumesnil, “Prosthetic heart valves: Selection of the optimal prosthesis and long-term management,” *Circulation*, vol. 119, no. 7, pp. 1034–1048, 2009.

[35] “Mechanical Heart Valves - Types: Bileaflet Valves.” [Online]. Available: http://www.pages.drexel.edu/~nag38/Types/bil.html. [Accessed: 04-Feb-2018].

[36] J. T. Ellis, T. M. Healy, A. A. Fontaine, R. Saxena, and A. P. Yoganathan, “Velocity measurements and flow patterns within the hinge region of a Medtronic Parallel bileaflet mechanical valve with clear housing.,” *J. Heart Valve Dis.*, vol. 5, no. 6, pp. 591–9, Nov. 1996.

[37] “An Update on Transcatheter Aortic Valve Replacement (TAVR) : Replacing the aortic valve without rib cracking - Medical Grapevine - medicalgrapevineasia.com.” [Online]. Available: http://www.medicalgrapevineasia.com/mg/2016/06/07/update-transcatheter-aortic-valve-replacement-tavr-replacing-aortic-valve-without-rib-cracking/. [Accessed: 04-Feb-2018].

[38] “Transcatheter aortic valve replacement (TAVR) - About - Mayo Clinic.” [Online]. Available: https://www.mayoclinic.org/tests-procedures/transcatheter-

aortic-valve-replacement/about/pac-20384698. [Accessed: 04-Feb-2018].

[39] “What is TAVR?” [Online]. Available: http://www.heart.org/HEARTORG/Conditions/More/HeartValveProblemsandDisease/What-is-TAVR_UCM_450827_Article.jsp#.WnekV6inHDc. [Accessed: 04-Feb-2018].

[40] R. Erbel, V. Aboyans, C. Boileau, E. Bossone, and R. Di Bartolomeo, “2014 ESC Guidelines on the diagnosis and treatment of aortic diseases,” *Jeroen J. Bax*.

[41] “Definition of Aorta.” [Online]. Available: https://www.medicinenet.com/script/main/art.asp?articlekey=2295. [Accessed: 06-Feb-2018].

[42] L. F. Hiratzka *et al.*, “ACCF/AHA Guideline 2010 ACCF/AHA/AATS/ACR/ASA/SCA/SCAI/SIR/STS/SVM Guidelines for the Diagnosis and Management of Patients With Thoracic Aortic Disease,” 2009.

[43] S. Verma and S. C. Siu, “Aortic Dilatation in Patients with Bicuspid Aortic Valve,” *N. Engl. J. Med.*, vol. 370, no. 20, pp. 1920–1929, 2014.

[44] T. M. Tadros, M. D. Klein, and O. M. Shapira, “Ascending aortic dilatation associated with bicuspid aortic valve. Pathophysiology, molecular biology, and clinical implications,” *Circulation*, vol. 119, no. 6, pp. 880–890, 2009.

[45] D. Lavall, H.-J. Schäfers, M. Böhm, and U. Laufs, “Aneurysms of the ascending aorta.,” *Dtsch. Arztebl. Int.*, vol. 109, no. 13, pp. 227–33, Mar. 2012.

[46] J. A. Elefteriades, “Thoracic Aortic Aneurysm: Reading the Enemy’s Playbook,” *Curr. Probl. Cardiol.*, vol. 33, no. 5, pp. 203–277, May 2008.

[47] E. Girdauskas *et al.*, “Functional Aortic Root Parameters and Expression of

Aortopathy in Bicuspid Versus Tricuspid Aortic Valve Stenosis," *J. Am. Coll. Cardiol.*, vol. 67, no. 15, pp. 1786–1796, 2016.

[48] M. A. Coady *et al.*, "What is the appropriate size criterion for resection of thoracic aortic aneurysms?," *J. Thorac. Cardiovasc. Surg.*, vol. 113, no. 3, pp. 476–491, Mar. 1997.

[49] "Thoracic Aortic Aneurysm Surgery | Cleveland Clinic: Health Library." [Online]. Available: https://my.clevelandclinic.org/health/treatments/17527-thoracic-aortic-aneurysm-surgery. [Accessed: 07-Feb-2018].

[50] "Endovascular Repair of AAA Society for Vascular Surgery." [Online]. Available: https://vascular.org/patient-resources/vascular-treatments/endovascular-repair-abdominal-aortic-aneurysms. [Accessed: 07-Feb-2018].

[51] "Left ventricular hypertrophy - Symptoms and causes - Mayo Clinic." [Online]. Available: https://www.mayoclinic.org/diseases-conditions/left-ventricular-hypertrophy/symptoms-causes/syc-20374314. [Accessed: 15-Apr-2018].

[52] M. Gaudino *et al.*, "Aortic Expansion Rate in Patients With Dilated Post-Stenotic Ascending Aorta Submitted Only to Aortic Valve Replacement," *J. Am. Coll. Cardiol.*, vol. 58, no. 6, pp. 581–584, Aug. 2011.

[53] E. Girdauskas *et al.*, "Functional Aortic Root Parameters and Expression of Aortopathy in Bicuspid Versus Tricuspid Aortic Valve Stenosis," *J. Am. Coll. Cardiol.*, vol. 67, no. 15, pp. 1786–1796, Apr. 2016.

[54] F. Robicsek, P. W. Sanger, F. H. Taylor, R. Magistro, and E. Fon, "Pathogenesis and Significance of Post-Stenotic Dilatation in Great Vessels *."

[55] O. E. Dapunt *et al.*, "The natural history of thoracic aortic aneurysms," *J. Thorac.*

Cardiovasc. Surg., vol. 107, pp. 1323–1333, 1994.

[56] Y. Hirose, S. Hamada, M. Takamiya, S. Imakita, H. Naito, and T. Nishimura, "Aortic aneurysms: growth rates measured with CT.," *Radiology*, vol. 185, no. 1, pp. 249–52, Oct. 1992.

[57] P. D. Stein and H. N. Sabbah, "Turbulent blood flow in the ascending aorta of humans with normal and diseased aortic valves.," *Circ. Res.*, vol. 39, no. 1, pp. 58–65, Jul. 1976.

[58] T. L. Yearwoodt, G. A. Misbacht, and K. B. Chandran#, "Experimental fluid dynamics of aortic stenosis in a model of the human aorta," *Clin. Phys. Physiol. Meas. Clin. Phys. Physiol. Meas. Clin. Phys. Physiol. Meas*, vol. 10, no. 1, pp. 11–24, 1989.

[59] A. P. Yoganathan, "Fluid mechanics of aortic stenosis," *Eur. Heart J.*, vol. 9, pp. 13–17, 1988.

[60] P. Van Ooij *et al.*, "Aortic Valve Stenosis Alters Expression of Regional Aortic Wall Shear Stress: New Insights From a 4-Dimensional Flow Magnetic Resonance Imaging Study of 571 Subjects."

[61] A. J. Barker *et al.*, "Bicuspid aortic valve is associated with altered wall shear stress in the ascending aorta.," *Circ. Cardiovasc. Imaging*, vol. 5, no. 4, pp. 457–66, Jul. 2012.

[62] J. M. Dolan, H. Meng, S. Singh, R. Paluch, and J. Kolega, "High Fluid Shear Stress and Spatial Shear Stress Gradients Affect Endothelial Proliferation, Survival, and Alignment," *Ann. Biomed. Eng.*, vol. 39, no. 6, pp. 1620–1631, Jun. 2011.

[63] D. Bluestein and S. Einav, “The effect of varying degrees of stenosis on the characteristics of turbulent pulsatile flow through heart valves,” *J. Biomech.*, vol. 28, no. 8, pp. 915–924, Aug. 1995.

[64] C. E. Seaman and P. Sucosky, “by,” no. April, 2014.

[65] A. Amindari, L. Saltik, K. Kirkkopru, M. Yacoub, and H. C. Yalcin, “Assessment of calcified aortic valve leaflet deformations and blood flow dynamics using fluid-structure interaction modeling,” *Informatics Med. Unlocked*, vol. 9, pp. 191–199, Jan. 2017.

[66] M. Kupari, H. Turto, and J. Lommi, “Left ventricular hypertrophy in aortic valve stenosis: Preventive or promotive of systolic dysfunction and heart failure?,” *Eur. Heart J.*, vol. 26, no. 17, pp. 1790–1796, 2005.

[67] T. Wada, M. D. McKee, S. Steitz, and C. M. Giachelli, “Calcification of vascular smooth muscle cell cultures: inhibition by osteopontin.,” *Circ. Res.*, vol. 84, no. 2, pp. 166–78, Feb. 1999.

[68] J. T. Butcher *et al.*, “Transcriptional profiles of valvular and vascular endothelial cells reveal phenotypic differences: influence of shear stress.,” *Arterioscler. Thromb. Vasc. Biol.*, vol. 26, no. 1, pp. 69–77, Jan. 2006.

[69] J. Richards *et al.*, “Side-Specific Endothelial-Dependent Regulation of Aortic Valve Calcification: Interplay of Hemodynamics and Nitric Oxide Signaling,” *Am. J. Pathol.*, vol. 182, no. 5, pp. 1922–1931, May 2013.

[70] K. Balachandran, P. Sucosky, and A. P. Yoganathan, “Hemodynamics and Mechanobiology of Aortic Valve Inflammation and Calcification,” vol. 2011, 2011.

[71] B. J. Ballermann, A. Dardik, E. Eng, and A. Liu, “Shear stress and the endothelium,” 1998.

[72] J.-J. Chiu and S. Chien, “Effects of disturbed flow on vascular endothelium: pathophysiological basis and clinical perspectives.,” *Physiol. Rev.*, vol. 91, no. 1, pp. 327–87, Jan. 2011.

[73] P. F. Davies, A. Remuzzitt, E. J. Gordon, C. F. Dewey, and M. A. Gimbrone, “Turbulent fluid shear stress induces vascular endothelial cell turnover in vitro (hemodynamic forces/endothelial growth control/atherosclerosis),” *Cell Biol.*, vol. 83, pp. 2114–2117, 1986.

[74] P. D. Stein and H. N. Sabbah, “Turbulent blood flow in the ascending aorta of humans with normal and diseased aortic valves,” *Circ. Res.*, vol. 39, no. 1, pp. 58–65, 1976.

[75] W. David Merryman, “Mechano-potential etiologies of aortic valve disease.,” *J. Biomech.*, vol. 43, no. 1, pp. 87–92, Jan. 2010.

[76] N. Saikrishnan, C.-H. Yap, N. C. Milligan, N. V. Vasilyev, and A. P. Yoganathan, “In Vitro Characterization of Bicuspid Aortic Valve Hemodynamics Using Particle Image Velocimetry,” *Ann. Biomed. Eng.*, vol. 40, no. 8, pp. 1760–1775, 2012.

[77] “the Effect of Shear Stress Magnitude on Aortic Valve,” *Cytokines*, no. April, 2010.

[78] A. P. Yoganathan, “Fluid mechanics of aortic stenosis,” *Eur. Heart J.*, vol. 9, no. suppl E, pp. 13–17, Apr. 1988.

[79] A. McNally, A. Madan, and P. Sucosky, “Morphotype-Dependent Flow Characteristics in Bicuspid Aortic Valve Ascending Aortas: A Benchtop Particle

Image Velocimetry Study.," *Front. Physiol.*, vol. 8, p. 44, 2017.

[80] J. Chambers, "The left ventricle in aortic stenosis: evidence for the use of ACE inhibitors.," *Heart*, vol. 92, no. 3, pp. 420–3, Mar. 2006.

[81] J. D. Humphrey, M. A. Schwartz, G. Tellides, and D. M. Milewicz, "Role of mechanotransduction in vascular biology: focus on thoracic aortic aneurysms and dissections.," *Circ. Res.*, vol. 116, no. 8, pp. 1448–61, Apr. 2015.

[82] B. Smith and D. Neal, "Particle Image Velocimetry," *Clim. Chang. 2013 - Phys. Sci. Basis*, vol. 53, pp. 1–30, 1989.

[83] J. Westerweet, "Digital Particle Image Velocimetry -Theory and Application."

[84] M. T. Lu, S. R. Thadani, and M. D. Hope, "Quantitative Assessment of Asymmetric Aortic Dilation with Valve-related Aortic Disease," *Acad. Radiol.*, vol. 20, no. 1, pp. 10–15, Jan. 2013.

[85] "20.2 Blood Flow, Blood Pressure, and Resistance | Anatomy & Physiology." [Online]. Available: http://library.open.oregonstate.edu/aandp/chapter/20-2-blood-flow-blood-pressure-and-resistance/. [Accessed: 01-Apr-2018].

[86] L. Zheng *et al.*, "Pulse pressure and mean arterial pressure in relation to ischemic stroke among patients with uncontrolled hypertension in rural areas of China.," *Stroke*, vol. 39, no. 7, pp. 1932–7, Jul. 2008.

[87] A. G. Wallace, J. H. Mitchell, N. S. Skinner, and S. J. Sarnoff, "Duration of the Phases of Left Ventricular Systole."

[88] R. Sarnari, R. Y. Kamal, M. K. Friedberg, and N. H. Silverman, "Doppler Assessment of the Ratio of the Systolic to Diastolic Duration in Normal Children: Relation to Heart Rate, Age and Body Surface Area," *J. Am. Soc. Echocardiogr.*,

vol. 22, no. 8, pp. 928–932, Aug. 2009.

[89] A. Amindari, L. Saltik, K. Kirkkopru, M. Yacoub, and H. C. Yalcin, “Assessment of calcified aortic valve leaflet deformations and blood flow dynamics using fluid-structure interaction modeling,” 2017.

[90] P. van Ooij *et al.*, “Aortic valve stenosis alters expression of regional aortic wall shear stress: New insights from a 4-dimensional flow magnetic resonance imaging study of 571 subjects,” *J. Am. Heart Assoc.*, vol. 6, no. 9, pp. 1–14, 2017.

[91] F. von Knobelsdorff-Brenkenhoff *et al.*, “Evaluation of Aortic Blood Flow and Wall Shear Stress in Aortic Stenosis and Its Association With Left Ventricular Remodeling.,” *Circ. Cardiovasc. Imaging*, vol. 9, no. 3, p. e004038, Mar. 2016.

[92] P. F. Davies, “Hemodynamic shear stress and the endothelium in cardiovascular pathophysiology.,” *Nat. Clin. Pract. Cardiovasc. Med.*, vol. 6, no. 1, pp. 16–26, Jan. 2009.

[93] M. Kupari, H. Turto, and J. Lommi, “Left ventricular hypertrophy in aortic valve stenosis: preventive or promotive of systolic dysfunction and heart failure?,” *Eur. Heart J.*, vol. 26, no. 17, pp. 1790–1796, Sep. 2005.